Molecular Therapy
Original Article

Dual CRALBP isoforms unveiled: iPSC-derived retinal modeling and AAV2/5-RLBP1 gene transfer raise considerations for effective therapy

Krishna Damodar,[1,7] Gregor Dubois,[1,7] Laurent Guillou,[1] Daria Mamaeva,[1] Marie Pequignot,[1] Nejla Erkilic,[1,2] Carla Sanjurjo-Soriano,[1] Hassan Boukhaddaoui,[1] Florence Bernex,[3] Béatrice Bocquet,[1,2] Jérôme Vialaret,[1,4] Yvan Arsenijevic,[5] T. Michael Redmond,[6] Christopher Hirtz,[1,4] Isabelle Meunier,[1,2] Philippe Brabet,[1] and Vasiliki Kalatzis[1,2]

[1]Institute for Neurosciences of Montpellier (INM), University of Montpellier, Inserm, 34091 Montpellier, France; [2]National Reference Centre for Inherited Sensory Diseases, University of Montpellier, Montpellier University Hospital, 34090 Montpellier, France; [3]RHEM, Réseau d'Histologie Expérimentale de Montpellier, University of Montpellier, Biocampus, CNRS, Inserm, 34298 Montpellier, France; [4]IRMB-PPC, INM, Montpellier University Hospital, Inserm, CNRS, University of Montpellier, 34295 Montpellier, France; [5]Unit of Retinal Degeneration and Regeneration, Department of Ophthalmology, University Lausanne, Jules-Gonin Eye Hospital, Fondation Asile des Aveugles, 1004 Lausanne, Switzerland; [6]Laboratory of Retinal Cell and Molecular Biology, National Eye Institute, National Institutes of Health, Bethesda, MD 20892, USA

Inherited retinal diseases (IRDs) are characterized by progressive vision loss. There are over 270 causative IRD genes, and variants within the same gene can cause clinically distinct disorders. One example is *RLBP1*, which encodes CRALBP. CRALBP is an essential protein in the rod and cone visual cycles that take place primarily in the retinal pigment epithelium (RPE) but also in Müller cells of the neuroretina. *RLBP1* variants lead to three clinical subtypes: Bothnia dystrophy, retinitis punctata albescens, and Newfoundland rod-cone dystrophy. We modeled *RLBP1*-IRD subtypes using patient-specific induced pluripotent stem cell (iPSC)-derived RPE and identified pathophysiological markers that served as pertinent therapeutic read-outs. We developed an AAV2/5-mediated gene-supplementation strategy and performed a proof-of-concept study in the human models, which was validated *in vivo* in an *Rlbp1*$^{-/-}$ murine model. Most importantly, we identified a previously unsuspected smaller CRALBP isoform that is naturally and differentially expressed both in the human and murine retina. This previously unidentified isoform is produced from an alternative methionine initiation site. This work provides further insights into CRALBP expression and *RLBP1*-associated pathophysiology and raises important considerations for successful gene-supplementation therapy.

INTRODUCTION

Light absorption by the retina initiates a series of chemical and electrical signals that are transmitted to the brain to create visual perception.[1] The light-sensitive retinal cells are the rod and cone photoreceptors. In the human retina, rods are preferentially located peripherally and are active in dim light, while cones are preferentially located centrally and are active in bright light. Inherited retinal diseases (IRDs) are a group of disorders characterized by photoreceptor degeneration and a progressive loss of vision.[2] They are clinically heterogeneous, with peripheral (rod loss) or central (cone loss) vision loss and have variable ages of onset and severity. IRDs are linked to variants in over 270 genes, which are important for the photoreceptors and/or the underlying support tissue, the retinal pigment epithelium (RPE). Furthermore, variants in the same gene can give rise to clinically distinct disorders.

One such example is the *RLBP1* gene. *RLBP1* variants are associated with the autosomal recessive IRD, retinitis punctata albescens (RPA; OMIM: 136880).[3–5] RPA is characterized by childhood-onset night blindness, elevated dark-adaptation thresholds, and uniform white dots across the fundus. The disease progresses to a generalized atrophy of the retina and macula (cone-rich center), leading to severe visual impairment from 40 years of age. *RLBP1* variants are also associated with two more severe clinical subtypes[6]: Bothnia dystrophy (BD; OMIM: 607475), which is characterized by an early involvement of the macula,[7,8] and Newfoundland rod-cone dystrophy (NFRCD; OMIM: 607476), characterized by night blindness from infancy and severe vision loss from 20 years of age.[9] In addition, *RLBP1* variants have been associated with a stationary form of night blindness, fundus albipunctatus (OMIM: 136880), which likely represents a mis-diagnosis of slowly progressive RPA in young patients.[10]

RLBP1 encodes the cellular retinaldehyde-binding protein (CRALBP).[11] CRALBP is an essential protein in the classic visual

Received 15 July 2024; accepted 4 October 2024;
https://doi.org/10.1016/j.ymthe.2024.10.004.

[7]These authors contributed equally

Correspondence: Vasiliki Kalatzis, INM, Inserm U1298, Hopital Saint-Eloi, BP 74103, 80 Avenue Augustin Fliche, 34091 Montpellier, France
E-mail: vasiliki.kalatzis@inserm.fr

cycle that occurs in the RPE to regenerate the visual chromophore 11-*cis*-retinal following light absorption.[12] In photoreceptor outer segments (POS), 11-*cis*-retinal is bound to rhodopsin and cone opsins. Following photon absorption, the chromophore is photoisomerized and transferred to the RPE to be recharged by a series of key steps: esterification to all-*trans*-retinyl esters by lecithin retinol acyltransferase (LRAT), isomerization to 11-*cis*-retinol by RPE65, and oxidation to light-sensitive 11-*cis*-retinal by the retinal dehydrogenases (RDHs). The rate-limiting step of the visual cycle is the isomerization by RPE65.[13–15] CRALBP is thought to accelerate this step by binding 11-*cis*-retinol to prevent reisomerization and/or binding photoreactive 11-*cis*-retinal for delivery to the POS via the interphotoreceptor retinoid-binding protein (IRBP).[16]

The classic visual cycle supports the majority of chromophore regeneration in both rods and cones. A secondary visual cycle in the Müller glial cells of the neuroretina, which also express CRALBP, was reported to specifically enable cones to quickly recover from bright light exposure.[17,18] Furthermore, CRALBP was recently shown to cooperate with the photoisomerase retinal G-protein-coupled receptor (RGR) in both the RPE and Müller glia in a rapid photic visual cycle that supplies both the central and peripheral retina.[19] CRALBP acts to selectively capture 11-*cis*-retinal produced by RGR, thus stimulating its activity. Taken together, CRALBP is essential for visual cycle kinetics in both rod- and cone-mediated vision.[16,20]

Currently no universal treatment exists for IRDs, but some patients have benefited from gene-supplementation clinical trials.[21] The treatment of IRDs due to a visual cycle defect became a reality when Luxturna, an adenovirus-associated virus serotype 2 (AAV2/2) vector carrying *RPE65* under the control of the strong CAG promoter, was market approved.[22] RPE65 deficiency causes all-*trans*-retinyl ester accumulation, leading to delayed or no 11-*cis*-retinal production.[23] This is quite similar to the effect of CRALBP deficiency,[16] but more severe. Thus, considering the success of Luxturna, RPA represented an excellent candidate for gene therapy. In this context, in 2015, Choi et al. reported that a self-complementary AAV2/8 vector expressing *RLBP1* under a short version of the endogenous human promoter (hRLBP1) improved the rate of dark adaptation in the *Rlbp1*$^{-/-}$ mouse model,[24] leading to the initiation of a clinical trial (NCT03374657) in 2018, the results of which are as yet unpublished.

In parallel, as we previously showed that AAV2/5 is the most effective serotype at transducing human RPE,[25] we conducted a separate proof-of-concept study with an AAV2/5 vector expressing *RLBP1* under the control of the CAG promoter. To ensure clinical relevance, we first modeled *RLBP1*-associated IRDs by generating induced pluripotent stem cell (iPSC)-derived RPE from patients carrying *RLBP1* variants associated with RPA, BD, and NFRCD. We assessed the effect of these variants on CRALBP expression and RPE function to identify pertinent read-outs for evaluating therapeutic rescue. We then performed proof-of-concept experiments for AAV2/5-mediated *RLBP1* supplementation *ex vivo* in the *RLBP1* iPSC-derived RPE and *in vivo* in the *Rlbp1*$^{-/-}$ mouse model. Interestingly and unexpectedly, this proof-of concept study has brought to light findings regarding CRALBP. We show here that the functionally validated AAV2/5-CAG-RLBP1 vector encodes two CRALBP isoforms. Moreover, we show that these isoforms are naturally and differentially expressed both in the human and murine retina. Finally, we demonstrate that the smaller isoform is produced from a second methionine codon. Taken together, this work provides further insights into CRALBP expression and *RLBP1*-associated pathophysiology and raises important considerations for successful gene-supplementation therapy.

RESULTS

Functionality of *RLBP1* iPSC-derived RPE correlates with clinical severity

To model *RLBP1*-associated IRDs, and to generate a pertinent human model for proof-of-concept studies, we cultured skin fibroblasts from *RLBP1* patients presenting with different clinical subtypes[6]: a 32-year-old woman (referred to as RPA1) with BD (Figure 1A), a 14-year-old boy (RPA2) with classic RPA (Figure 1B), and a 31-year-old man (RPA3) with severe NFRCD (Figure 1C). We reprogrammed the fibroblasts into iPSCs, which were quality controlled for Sendai vector clearance by RT-PCR (Figure S1A), pluripotency by qPCR (Figure S1B), trilineage differentiation by teratoma assay (Figure S1C), and genetic integrity by karyotype analysis (Figure S1D). Furthermore, we screened for the presence of the causative *RLBP1* variants by PCR amplification and Sanger sequencing. We detected the c.333T>G (p.Tyr111*) variant in exon 5 and c.700C>T (p.Arg234Trp) in exon 8 in RPA1 iPSCs (Figure 1D), and c.25C>T (p.Arg9Cys) in exon 4 and c.333T>G in exon 5 in RPA2 iPSCs (Figure 1E). In addition, using long-range PCR analysis, we detected a 300-bp fragment corresponding to the homozygous exon 7–9 deletion[3] in RPA3 iPSCs (Figure 1F), compared to an ∼8-kb fragment in control iPSCs. The position of the variants on the *RLBP1* gene are schematized in Figure 1G.

We then differentiated control[26] and *RLBP1* iPSC lines into RPE. Using immunofluorescence (IF) studies, we detected expression of characteristic markers in all patient lines: the apical adherens marker ZO-1 (Figure 2A); the basolateral chloride channel Bestrophin-1 (Figure 2B); the perinuclear and cytosolic visual cycle markers LRAT (Figure 2B) and RPE65 (Figure 2C), respectively; and the apical microvilli marker MERTK (Figure 2C); representative data are shown for the severe RPA3 line. Trans-epithelial resistance (TER) recordings increased weekly for the control and patient iPSC-derived RPE, reaching values >150 Ω/cm^2 (Figure 2D), indicative of a tight monolayer.[27] We assayed the general functionality of the iPSC-derived RPE by feeding with FITC-labeled POS and quantifying the percentage of fluorescent cells (Figure 2E) and their mean fluorescence intensity (Figure 2F) by flow cytometry. Overall, this characteristic function was not significantly different between control, RPA1, and RPA2 RPE, whereas RPA3 RPE showed significantly reduced phagocytosis compared to the other lines.

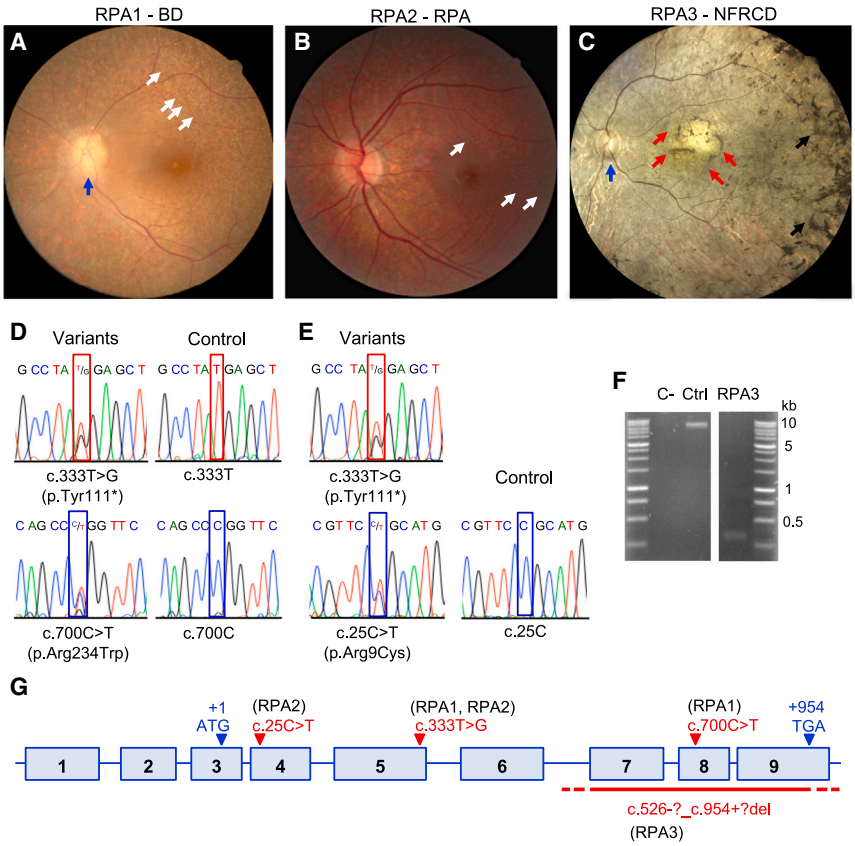

Figure 1. Clinical phenotype and genotype of *RLBP1* patients

Color fundus imaging of individual: RPA1 at 28 years of age presenting with BD showing multiple white dots (white arrows), an irregular pale optic nerve head with papillary drusen (blue arrow), and reduced retinal vessel caliber (A); RPA2 at 23 years of age presenting with mild RPA showing multiple white dots (white arrows) but preserved papillary head and retinal vessels (B); and RPA3 presenting with severe NFRCD at 45 years of age showing nummular pigmentary changes (black arrows), a pale optic nerve head (blue arrow), and an altered and atrophic macula (red arrows) (C). Sanger sequencing of the *RLBP1* variants c.333T>G and c.700C>T (D) and c.25C>T and c.333T>G (E) in the iPSCs of individuals RPA1 and RPA2, respectively. (F) Long-range PCR amplification of the region flanking the homozygous exon 7–9 deletion carried by RPA3. C-, water control; Ctrl, control DNA. (G) Schematic representation of *RLBP1* with the position of the variants carried by RPA1, RPA2, and RPA3 indicated in red; the positions of the start and stop codons are indicated in blue.

Taken together, iPSC-derived RPE from *RLBP1* patients presents a morphologically characteristic monolayer with altered functionality for the most severe clinical phenotype.

CRALBP expression in iPSC-derived RPE depends on the causative *RLBP1* variant

We next assayed *RLBP1* expression by qPCR using primers in exon 6 and detected expression in the control iPSC-derived RPE and not in undifferentiated iPSCs (Figure 3A). We detected significantly reduced *RLBP1* levels in the iPSC-derived RPE lines RPA1 (0.2-fold of control) and RPA2 (0.5-fold), which carried a combination of missense and nonsense alleles, and RPA3 (0.13-fold), which carried the large exon 7 to 9 deletion, compared to controls. This expression profile was confirmed using a second set of primers in different exons (Figure S2A). Consistent with varying mRNA levels between patients, western blot analysis of 10 µg of iPSC-derived RPE cell lysates detected CRALBP in RPA2 RPE, at 0.2-fold of control levels, but not in RPA3 RPE (Figure 3B). Surprisingly, CRALBP expression was not detected in RPA1 RPE.

We then performed IF studies to further verify CRALBP expression. In control iPSC-derived RPE, CRALBP staining was diffuse throughout the cytosol but highly concentrated on the inner side of the plasma membrane (Figure 3C), consistent with our previous reports.[26,28] Unexpectedly, in RPA1 RPE, CRALBP expression was faint and partially mis-localized; the staining was mainly diffuse in the cytosol and unevenly distributed near the plasma membrane (Figure 3D). By contrast, CRALBP expression in RPA2 RPE showed a similar pattern to control RPE, though less intense (Figure 3E). Consistent with the western blot data, CRALBP was not detected in RPA3 RPE (Figure 3F). Due to the discrepancy in CRALBP detection for RPA1 between the western blot analysis of RPE cultured in 24-well plates and the IF data for RPE cultured on Transwell inserts, we performed additional western blot analyses on iPSC-derived RPE cultured on inserts and directly resuspended in Laemmli buffer. Under these conditions, CRALBP was detectable at levels 0.3-fold of control (Figure 3G).

In conclusion, RPE from the BD and RPA patients shows reduced *RLBP1* expression but detectable CRALBP, whereas RPE from severe NFRCD has no detectable CRALBP.

RLBP1 iPSC-derived RPE shows retinoid accumulation

CRALBP is an 11-*cis*-retinoid-binding protein that drives the isomerization reaction carried out by RPE65.[29] We hence assayed retinoid accumulation in the RPE associated with the two most extreme clinical phenotypes, mild RPA (RPA2) and severe NFRCD (RPA3). To this end, we incubated iPSC-derived RPE with all-*trans*-retinol to mimic the visual cycle and measured all-*trans*-retinyl ester levels by high-performance liquid chromatography (HPLC). Both patient-derived RPE lines showed significantly higher all-*trans*-retinyl ester levels compared to control RPE (Figure 4A). Furthermore, in native RPE, retinoids accumulate in a specialized lipid droplet termed

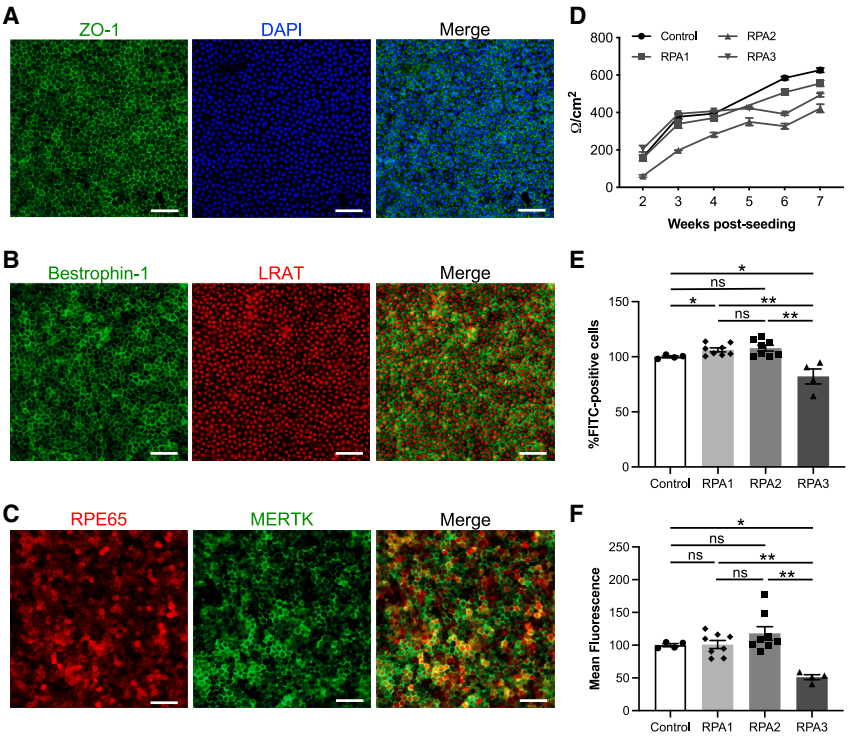

Figure 2. Morphological and functional characteristics of *RLBP1* iPSC-derived RPE

Representative IF images of the iPSC-derived RPE from patient RPA3 stained for the markers ZO-1 (A), Bestrophin-1 and LRAT (B), and RPE65 and MERTK (C); nuclei are stained in blue. Scale bars, 50 μm. (D) Weekly TER measurements of control, RPA1, RPA2, and RPA3 iPSC-derived RPE expressed in ohms/cm^2. Data are represented as mean ± SEM of recordings from five inserts (control and RPA1) or six inserts (RPA2 and RPA3). Flow cytometry analysis of the percentage of iPSC-derived RPE cells that phagocytosed FITC-labeled POS (E) and the mean fluorescence intensity following phagocytosis (F) expressed relative to control. Data are represented as mean ± SEM; *$p < 0.05$; **$p < 0.01$; ns, non-significant; $n = 4$ (control and RPA3) and 8 (RPA1 and RPA2); Mann-Whitney test.

a retinosome,[30] which can be visualized by transmission electron microscopy (TEM). We performed TEM analysis and observed a similar polarized structure (apical microvilli, basal nuclei) in both control and patient iPSC-derived RPE. By contrast, intracellular droplets were readily visible in RPA2 and RPA3 RPE as opposed to control tissue (Figure 4B). The number of droplets was significantly higher from 2 months post seeding (Figure 4C). Furthermore, with prolonged culture (up to 7 months post seeding), the number of droplets increased 2.3-fold and remained significantly more abundant than in control RPE.

Retinosomes can also be detected using multiphoton microscopy from wavelengths 720–780 nm.[31] Multiphoton microscopy of iPSC-derived RPE readily detected fluorescent vesicles that appeared larger in RPA2 and RPA3 RPE compared to control tissue (Figure 4D). We quantified the area of fluorescence and confirmed a significant increase in the *RLBP1* RPE (Figure 4E). To definitively identify the lipid droplets as retinosomes, we tested for the expression of the specific marker perilipin-2 by western blot analysis and detected significantly higher levels in RPA2 and RPA3 RPE compared to control tissue (Figure 4F). As we had access to the *Rlbp1*$^{-/-}$ mouse model (see below), we further validated these findings by western blot analysis of murine RPE, where we detected significantly higher perilipin-2 levels in *Rlbp1*$^{-/-}$ mice compared to wild type (Figure 4G). We previously showed that retinosome accumulation could be associated with defective polarized secretion in iPSC-derived RPE from *TBC1D32*-associated IRD.[28] To investigate similar patterns in *RLBP1* RPE, we assayed vascular endothelial growth factor (VEGF), which is primarily secreted basally, and pigment epithelium-derived factor (PEDF), which is primarily secreted apically.[32] We did not detect significant differences in basal VEGF and apical PEDF secretion between control, RPA2, and RPA3 RPE (Figure 4H). However, we detected significantly elevated VEGF secretion apically in RPA3 RPE and a significantly reduced PEDF secretion basally in RPA2 and RPA3 RPE compared to controls.

Taken together, the RPE from *RLBP1* patients exhibits clear retinosome accumulation, which could serve as a potential therapeutic readout.

AAV-RLBP1 encodes two CRALBP isoforms that are native to the mammalian RPE

We previously showed that AAV2/5 is the most effective serotype at transducing human RPE.[25] Consequently, we designed an AAV2/5 vector carrying *RLBP1* under the control of the CAG promoter (AAV-RLBP1). To perform a proof-of-concept gene-supplementation study with clinical translatability, we subcloned the transgene cassette into two essentially identical proviral plasmids, pDDO and pKL. The difference between them is that pKL is more suitable for clinical development due to the larger distance between the kanamycin resistance cassette and the 5′ inverted terminal repeat (ITR). After transfecting the plasmids into COS-7 cells, we confirmed *RLBP1* expression by qPCR analysis using a forward primer spanning the exon 6 to 7 junction and a reverse primer in exon 7 (Figure 5A), and CRALBP expression by IF studies (Figure 5B) and western blot analysis (Figure 5C). Unexpectedly, we detected a specific signal migrating at the expected size of 36 kDa but composed of two bands (Figure 5C), regardless of the proviral plasmid and the intronless *RLBP1* cassette. To rule out technical issues, we repeated western blot analysis using different lysis conditions (Figure S2B) but consistently observed two CRALBP bands. We also tested denaturing versus

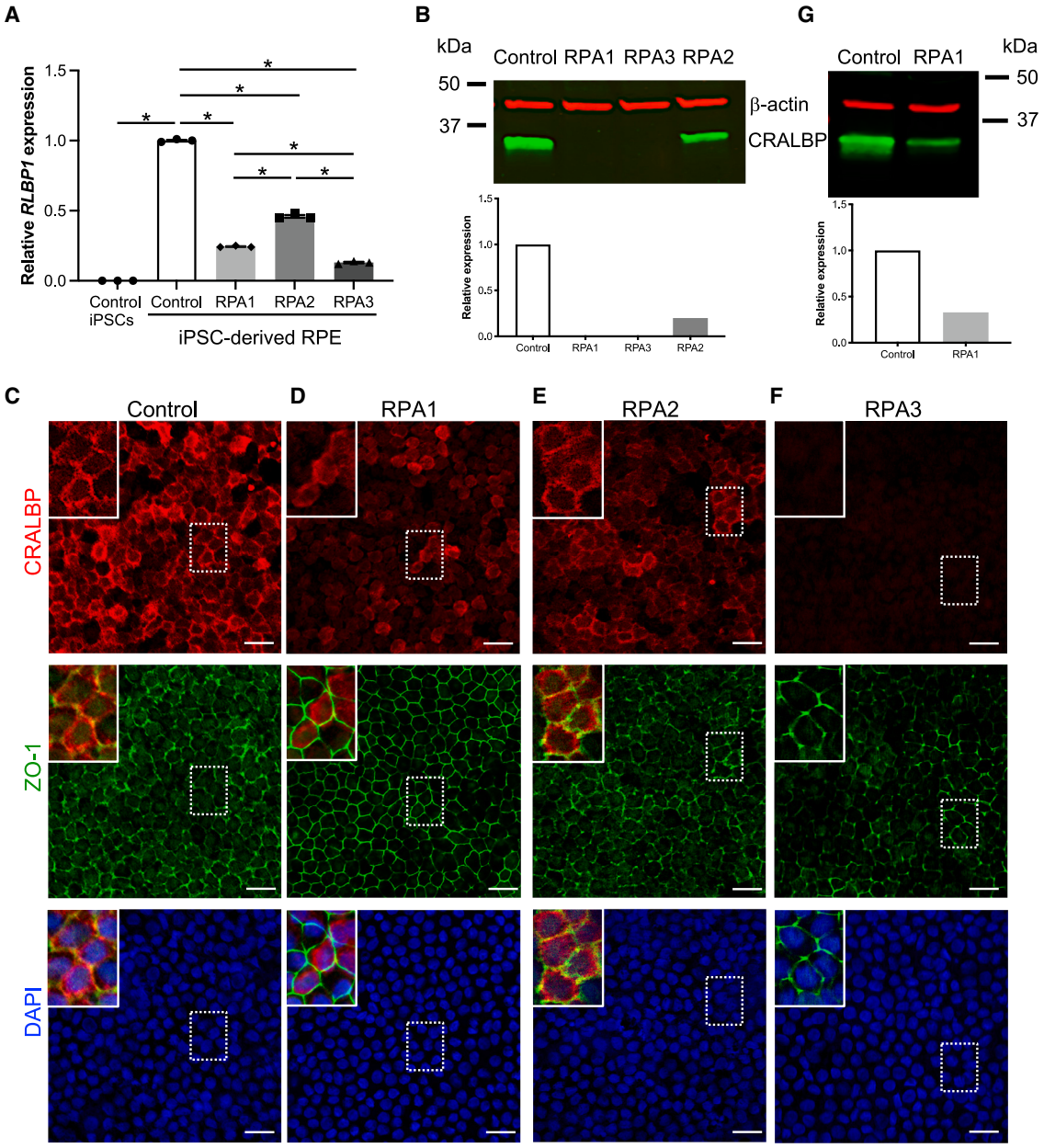

Figure 3. *RLBP1* and CRALBP expression in iPSC-derived RPE

(A) qPCR analysis of *RLBP1* expression in control iPSCs, and control and patient iPSC-derived RPE. Data are represented as mean ± SEM and expressed relative to control; $^*p < 0.05$; $n = 3$; Mann-Whitney test. (B) Western blot analysis of CRALBP expression (green) in control and patient iPSC-derived RPE cell lysates. The graphs represent the quantification of CRALBP relative to the loading control, β-actin (red). Representative IF images of control (C), RPA1 (D), RPA2 (E), and RPA3 (F) iPSC-derived RPE stained for CRALBP and ZO-1 and shown as individual channels; nuclei are labeled in blue. Scale bars, 20 μm. Insets, 2-fold magnification of the boxed areas for each panel shown as merged images with the preceding channel (top row, red alone; middle row, red and green; bottom row, red, green, and blue). (G) Western blot analysis of CRALBP expression in control and RPA1 iPSC-derived RPE cultured on Transwell inserts. The graph represents the quantification of CRALBP relative to the loading control, β-actin.

native conditions using a mouse monoclonal or polyclonal anti-CRALBP antibody. Under denaturing conditions, both monoclonal (Figure S2C) and polyclonal (not shown) antibodies detected two bands, although the polyclonal antibody gave high background. Under native conditions, the two CRALBP bands were highly resolved and more or less detectable, depending on the lysis buffer, using the polyclonal antibody (Figure S2D) but not the monoclonal antibody (not shown).

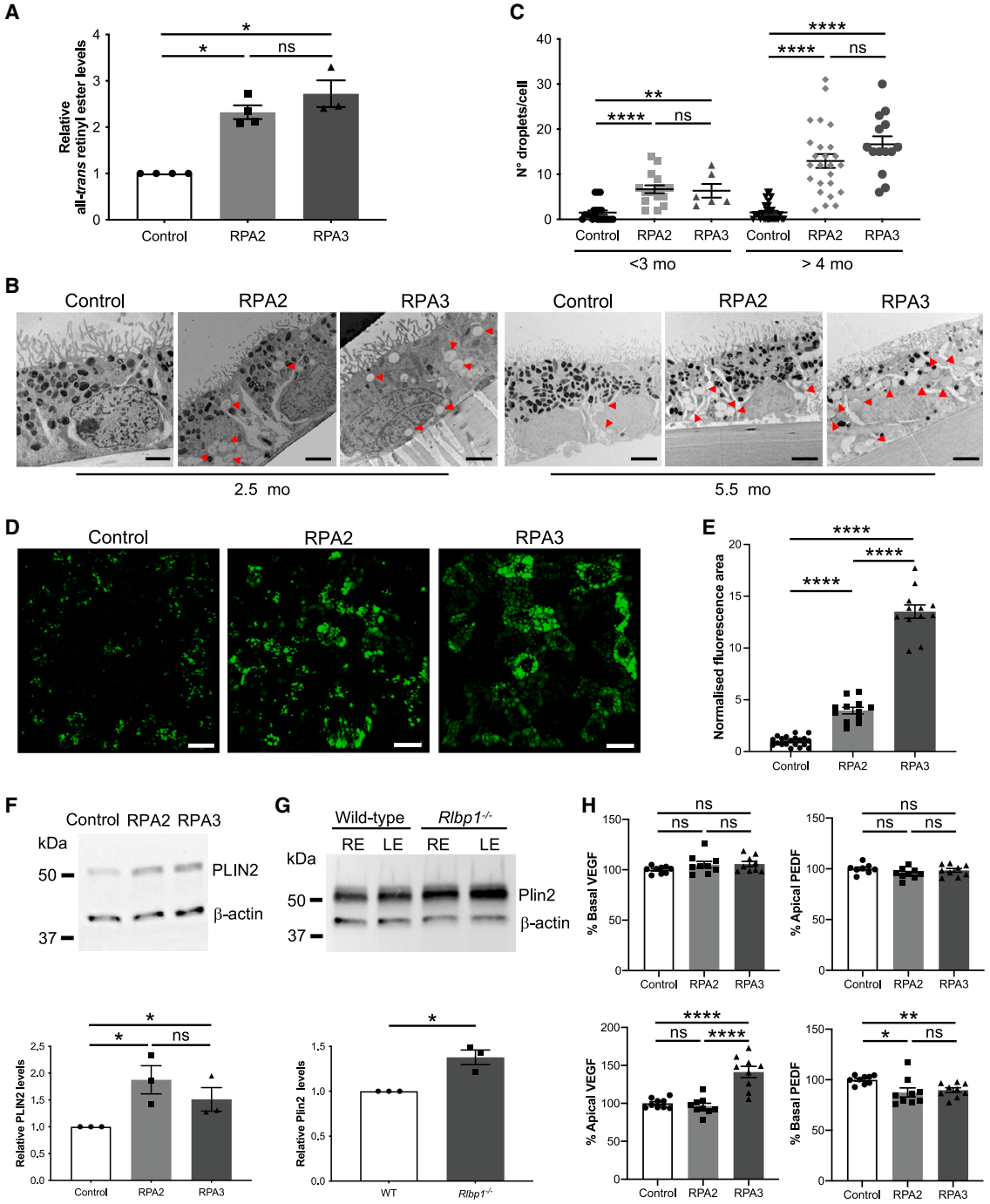

Figure 4. Retinosome accumulation and polarized secretion in iPSC-derived RPE

(A) HPLC of all-*trans*-retinyl ester levels in control, RPA2, and RPA3 RPE expressed as fold increase over control. Data are represented as mean ± SEM; *$p < 0.05$; ns, non-significant; $n = 4$ (control and RPA2) and 3 (RPA3); Mann-Whitney test. (B) Representative TEM images of control, RPA2, and RPA3 iPSC-derived RPE at 2.5 and 5.5 months (mo) post seeding. Lipid droplets are indicated by red arrowheads. Scale bars, 2 μm. (C) Quantitative analysis of the number of droplets/cell following TEM analysis of control and patient iPSC-derived RPE grouped according to age post seeding. Data are represented as mean ± SEM; **$p < 0.01$; ****$p < 0.0001$; ns, non-significant; $n = 20$ (control), 16 (RPA2), and 6 (RPA3) for <3 months and $n = 28$ (control), 25 (RPA2), and 14 (RPA3) for >4 months; Mann-Whitney test. (D) Representative images of multiphoton microscopy of fluorescent retinosomes in control and patient iPSC-derived RPE at 7 months post seeding. Scale bars, 15 μm. (E) Quantitative analysis of the area of fluorescence normalized to the area of the image. Data are represented as mean ± SEM; ****$p < 0.0001$; $n = 20$ (control) and 12 (RPA2 and RPA3); Student's t test.

(legend continued on next page)

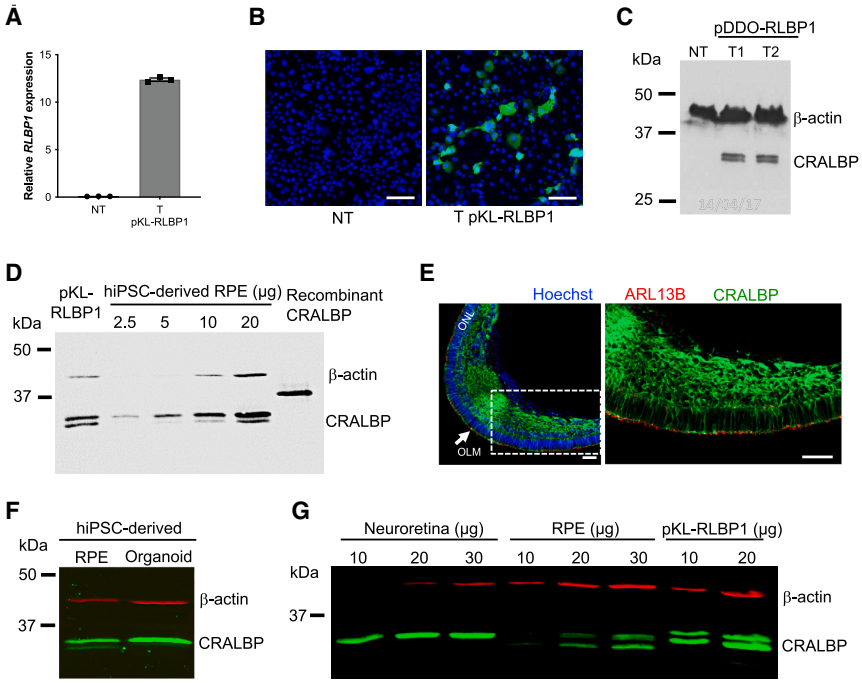

Figure 5. Unveiling of dual CRALBP isoforms

(A) qPCR analysis of *RLBP1* expression in COS-7 non-transfected (NT) or transfected (T) with pKL-RLBP1. Data are represented as mean ± SEM. (B) IF studies of CRALBP in NT and T COS-7 cells using a mouse monoclonal anti-CRALBP antibody. Scale bars, 50 µm. (C) Western blot analysis of CRALBP in NT and COS-7 cells transfected (T1 and T2) with pDDO-RLBP1; β-actin represents the loading control. (D) Western blot analysis of CRALBP in human iPSC-derived RPE at different loading levels. Positive controls, COS-7 cells transfected with pKL-RLBP1 and 200 ng of recombinant CRALBP protein; β-actin represents the loading control. (E) CRALBP and ARL13B in human iPSC-derived retinal organoids at differentiation day 225; nuclei are labeled in blue. ONL, outer nuclear layer; OLM, outer limiting membrane (arrow). The right panel is a magnification of the region boxed in the left panel without the blue channel. Scale bars, 50 µm. (F) Western blot analysis of CRALBP in human iPSC-derived RPE and retinal organoids; β-actin represents the loading control. (G) Western blot analysis of CRALBP in the neuroretina and RPE of wild-type mice; HEK293 cells transfected with pKL-RLBP1 were used as a positive control for the double band profile; β-actin represents the loading control.

To determine if the two CRALBP isoforms observed were a consequence of *RLBP1* overexpression, we examined endogenous CRALBP by western blot analysis of healthy iPSC-derived RPE on a high-resolution (15%) polyacrylamide gel. We clearly detected two bands of the same size as those observed in transfected cells, with band intensity increasing proportionally to protein loading (Figure 5D). This confirmed that the two isoforms were native to human RPE; the His-tagged recombinant CRALBP protein, used as a control, migrated at a higher molecular weight (predicted 37.4 kDa). Next, we investigated whether the two CRALBP isoforms were also present in human Müller cells of the neuroretina, which express *RLBP1*. We thus analyzed healthy human iPSC-derived retinal organoids without RPE by IF studies and detected CRALBP in the prolongations of the Müller cells throughout the outer nuclear layer and in the Müller endfeet forming the outer limiting membrane (Figure 5E). By western blot analysis, we only detected the larger CRALBP isoform in the retinal organoids, in contrast to the RPE (Figure 5F). To further validate that CRALBP expression in the human iPSC-derived retinal tissues reflects the *in vivo* situation, we tested Cralbp expression in wild-type murine neuroretina and RPE separately. We clearly detected two Cralbp isoforms in murine RPE and exclusively detected the larger isoform in neuroretina (Figure 5G), thus confirming the results obtained in the human iPSC-derived models.

In conclusion, *RLBP1* produces two CRALBP isoforms in the RPE but only the larger canonical isoform in the neuroretina.

Smaller CRALBP isoform arises from an internal methionine codon

To determine the origin of the smaller CRALBP isoform, we initiated mass spectrometry proteomic analysis of recombinant CRALBP and COS-7 cells transfected with pKL-RLBP1. Analysis of three gel fractions spanning the area of both isoforms identified various peptide fragments corresponding to CRALBP (Figure S3A). Notably, N-terminal peptides containing the first nine amino acids (aa) of CRALBP were found only in the highest-molecular-weight (first) gel fraction, whereas N-terminal peptides beginning at a second methionine codon at aa position 10 were identified in the second and third fractions. These results suggested that differential initiation of translation from different methionine codons resulted in the two CRALBP isoforms. To confirm this, we performed site-directed mutagenesis to replace the methionine codons with alanine in pKL-RLBP1. We thus generated pKL-RLBP1-Met1Ala, mutated in the residue at position 1, and pKL-RLBP1-Met10Ala, mutated in the residue at position 10. After transfecting the plasmids in COS-7 cells and western blot analysis, we detected two CRALBP bands from the maternal plasmid (Figure 6A) and exclusively detected the smaller

(F) Representative western blot analysis of human perilipin-2 (PLIN2) expression in control, RPA2, and RPA3 iPSC-derived RPE; β-actin represents the loading control. Graph represents the quantification of PLIN2 normalized to β-actin and relative to control. Data are represented as mean ± SEM; $*p < 0.05$; ns, non-significant; $n = 3$; Mann-Whitney test. (G) Representative western blot analysis of murine perilipin-2 (Plin2) expression in the right (RE) and left (LE) eye of wild-type and *Rlbp1*$^{-/-}$ RPE; β-actin represents the loading control. Graph represents the quantification of Plin2 normalized to β-actin and relative to control. Data are represented as mean ± SEM; $*p < 0.05$; $n = 3$; Mann-Whitney test. (H) ELISA of VEGF and PEDF secreted apically and basally from iPSC-derived RPE. Data are represented as mean ± SEM and expressed as a percentage of control; $*p < 0.05$; $**p < 0.01$; $****p < 0.0001$; ns, non-significant; $n = 9$; Student's t test.

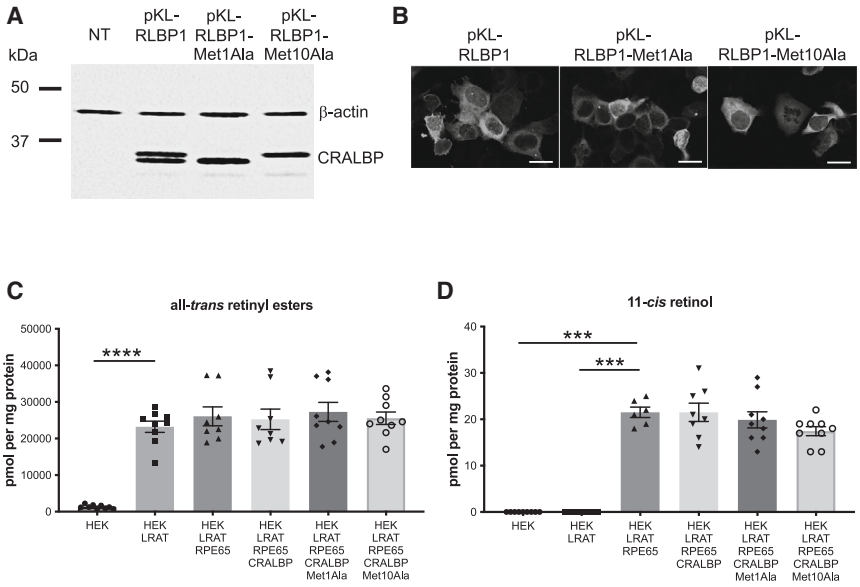

Figure 6. Origin and functional analysis of CRALBP isoforms

(A) Western blot analysis of CRALBP in COS-7 cells NT or transfected with the control or mutant (Met1Ala, Met10Ala) pKL-RLBP1 plasmids; β-actin represents the loading control. (B) IF studies of CRALBP expression in HEK293 cells transfected with the control or mutant pKL-RLBP1. Scale bars, 20 μm. HPLC analysis of all-*trans*-retinyl esters (C) and11-*cis*-retinol (D) levels (expressed in pmol per mg protein) in HEK293 cells transfected with LRAT, RPE65, and control or mutant CRALBP plasmids and incubated with all-*trans*-retinol. Data are represented as mean ± SEM. ***$p < 0.001$; ****$p < 0.0001$; *n* is indicated by the symbols.

band from pKL-RLBP1-Met1Ala and the larger band from pKL-RLBP1-Met10Ala. In addition, IF studies of transfected HEK293 cells detected CRALBP from each construct (Figure 6B).

In light of these findings, we repeated western blot analysis of the patient-specific iPSC-derived RPE to determine if both isoforms were present. At higher loading levels (30 μg), we observed two CRALBP bands in the RPE of RPA2 (Figure S3B); overexpression of the western blot shown in Figure 4G also suggested a second band in RPA1 RPE (not shown). To unequivocally determine whether the mutant alleles c.25C>T and c.700C>T carried by RPA2 and RPA1, respectively, expressed both CRALBP isoforms, we introduced these variants into pKL-RLBP1 by site-directed mutagenesis, transfected HEK293 cells, and performed western blot analysis. This confirmed the production of both isoforms (Figure S3C).

In the visual cycle, RPE65 activity is enhanced by CRALBP, likely by limiting the back inhibition of 11-*cis*-retinol, the product of the isomerization reaction.[12] To evaluate the impact of the two CRALBP isoforms on 11-*cis*-retinol production, we transfected a stable LRAT-expressing HEK293 cell line[33] with a plasmid expressing RPE65 alone or in combination with pKL-RLBP1, pKL-RLBP1-Met1Ala, or pKL-RLBP1-Met10Ala. We then initiated an artificial visual cycle by adding all-*trans*-retinol (vitamin A) to the transfected cells and assayed all-*trans*-retinyl ester and 11-*cis*-retinol production by HPLC. We confirmed that the LRAT-expressing cells produced significantly higher all-*trans*-retinyl ester levels compared to control cells (Figure 6C) due to the esterification of the exogenous all-*trans*-retinol. These levels were not significantly altered by the addition of the RPE65 or CRALBP plasmids. By comparison, 11-*cis*-retinol levels were only detected upon addition of RPE65 due to the isomerization reaction (Figure 6D). These levels showed a tendency to increase, which was not statistically significant, upon addition of both CRALBP isoforms. This may have been due to variations between RPE65 and CRALBP plasmid expression levels.[15] If we compare the cells transfected with the same plasmid expressing the different CRALBP isoforms, we did not detect significant differences in 11-*cis*-retinol levels when both isoforms were present together or each isoform was present individually.

Taken together, the smaller CRALBP isoform results from the differential use of a second methionine codon and may also be involved in the visual cycle.

AAV-RLBP1 reduces retinosome accumulation in *RLBP1* iPSC-derived RPE

We next conducted a proof-of-concept study using AAV-RLBP1 in functionally validated iPSC-derived RPE from patients RPA2 and RPA3 and assessed its efficacy by measuring retinosome accumulation. Western blot analysis performed 1 month post transduction clearly revealed the presence of two CRALBP bands (Figure 7A). Notably, CRALBP levels increased in RPA2 and RPA3 RPE post-transduction compared to untreated tissue. Moreover, perilipin-2 levels decreased in RPA2 and RPA3 RPE post AAV-RLBP1 transduction compared to untreated tissues (Figure 7B). To consolidate these results, we performed a quantitative TEM study of the number of droplets in non-transduced and transduced RPA2 and RPA3 RPE. We detected a significant decrease in the number of droplets in these tissues following AAV-RLBP1 transduction (Figure 7C).

In conclusion, we provide proof of concept for the efficacy of AAV-RLBP1 in a human context and demonstrate the value of using *RLBP1* iPSC-derived RPE as a model for evaluating therapeutic strategies.

AAV-RLBP1 improves visual cycle kinetics and retinal function in *Rlbp1*$^{-/-}$ mice

Lastly, we validated our *ex vivo* human AAV-RLBP1 proof-of-concept study using the *in vivo Rlbp1*$^{-/-}$ murine model, which was reported to show delayed visual cycle recovery following

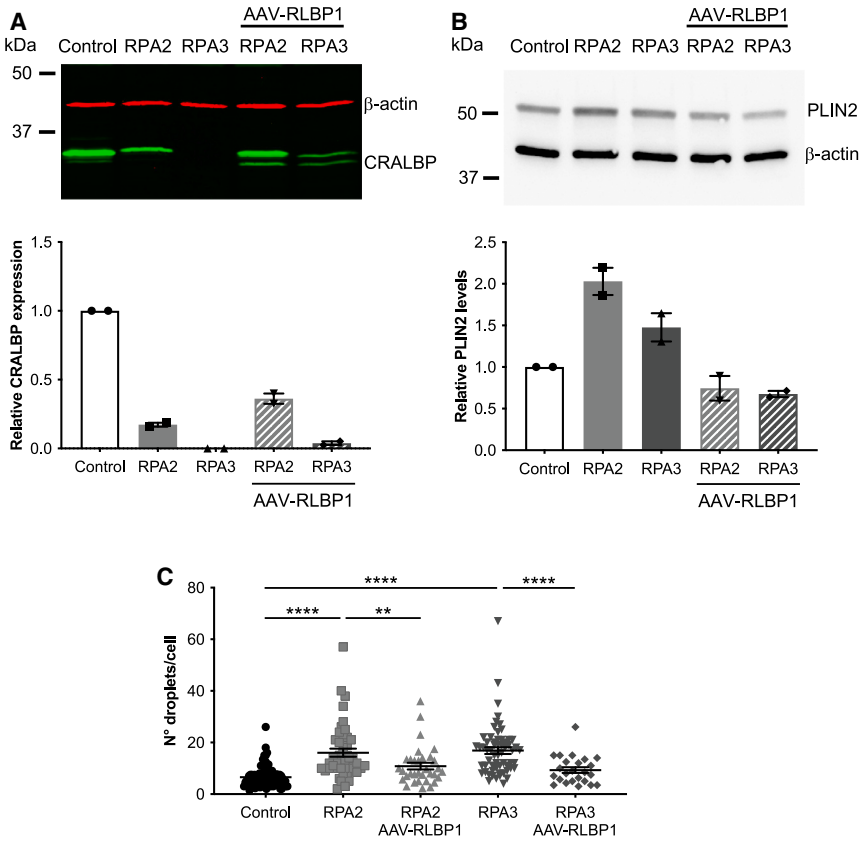

Figure 7. Rescue of retinosome accumulation in iPSC-derived RPE

(A) Representative western blot analysis of CRALBP in control RPE and non-transduced and AAV-RLBP1-transduced RPA2 and RPA3 RPE; β-actin represents the loading control. Graph represents the quantification of CRALBP normalized to β-actin and expressed relative to control in two independent experiments. Data are represented as mean ± SEM. (B) Representative western blot analysis of PLIN2 in control RPE and non-transduced and AAV-RLBP1-transduced RPA2 and RPA3 RPE; β-actin represents the loading control. Graph represents the quantification of PLIN2 normalized to β-actin and relative to control in two independent experiments. Data are represented as mean ± SEM. (C) Quantitative analysis of the number of droplets per cell following TEM analysis of control RPE and non-transduced and transduced RPA2 and RPA3 RPE. Data are represented as mean ± SEM; $^{**}p < 0.01$; $^{****}p < 0.0001$; $n = 81$ (control), 45 (RPA2), 33 (RPA2 AAV-RLBP1), 60 (RPA3), and 24 (RPA3 AAV-RLBP1); Mann-Whitney test.

photobleaching accompanied by an accumulation of all-*trans*-retinyl esters.[16] To facilitate subretinal injections, we first crossed the albino *Rlbp1*$^{-/-}$ mice onto a pigmented strain. We next administered AAV-RLBP1 and, 4-weeks post transduction, we verified human *RLBP1* expression by qPCR (Figure 8A) and CRALBP by western blot analysis using a low-resolution AnykD gel (Figure 8B). Under these migration conditions, the two CRALBP isoforms were not separated. We therefore confirmed production of both isoforms *in vivo* by additional western blot analysis following migration on a 15% polyacrylamide gel (Figure S4A). We then assayed the recovery of visual cycle kinetics following AAV-RLBP1 treatment of *Rlbp1*$^{-/-}$ mice by HPLC analysis of 11-*cis*-retinal (Figure 8C) and all-*trans*-retinyl ester (Figure 8D) levels. *Rlbp1*$^{-/-}$ mice were treated for up to 8 weeks with 5×10^8 vg, 1×10^9 vg, or 2×10^9 vg of AAV-RLBP1, or injected with Dulbecco's Phosphate-Buffered Saline (DPBS) or an AAV2/5-CAG vector expressing GFP (referred to as AAV-GFP) as surgical and vector controls, respectively. At the end of the treatment period, the experimental groups were photobleached, dark adapted, and the eyes were assayed for retinoid content.

Consistent with findings in the albino strain,[16] 11-*cis*-retinal production was significantly lower in pigmented non-injected, DPBS-, and AAV-GFP-injected *Rlbp1*$^{-/-}$ mice compared to wild-type mice (Figure 8C). No significant differences were detected between the three control *Rlbp1*$^{-/-}$ groups; therefore, comparisons post treatment with AAV-RLBP1 are shown relative to the AAV-GFP-injected group. After treatment with the low 5×10^8-vg dose of AAV-RLBP1, 11-*cis*-retinal levels in *Rlbp1*$^{-/-}$ mice remained significantly lower than those in wild-type mice and were not significantly different from the AAV-GFP-injected littermates. By contrast, treatment with the intermediate 1×10^9-vg and high 2×10^9-vg doses of AAV-RLBP1 resulted in significantly increased 11-*cis*-retinal levels compared to AAV-GFP-injected controls (Figure 8C), demonstrating a dose-dependent effect. Importantly, the levels post treatment were not significantly different from those in wild-type mice.

Regarding all-*trans*-retinyl esters, production was significantly higher in non-injected, DPBS-, and AAV-GFP-injected *Rlbp1*$^{-/-}$ mice compared to wild-type mice (Figure 8D). Treatment with 1×10^9 vg or 2×10^9 vg of AAV-RLBP1 resulted in significantly decreased all-*trans*-retinyl ester levels in *Rlbp1*$^{-/-}$ mice compared to AAV-GFP-injected littermates. Again, treatment with the lowest dose of 5×10^8 vg AAV-RLBP1 did not significantly alter all-*trans*-retinyl ester levels compared to AAV-GFP-injected controls. However, a trend toward reduced ester levels in the low-dose group was suggested by the lack of significant differences between the three doses. Importantly, all-*trans*-retinyl ester levels in *Rlbp1*$^{-/-}$ mice treated with all three doses of AAV-RLBP1 were not significantly different from wild-type levels (Figure 8D). Given that the intermediate 1×10^9-vg and highest 2×10^9-vg doses of AAV-RLBP1 showed the most consistent effects, and that no significant differences were found between those doses in terms of 11-*cis*-retinal (Figure 8C) or all-*trans*-retinyl ester (Figure 8D)

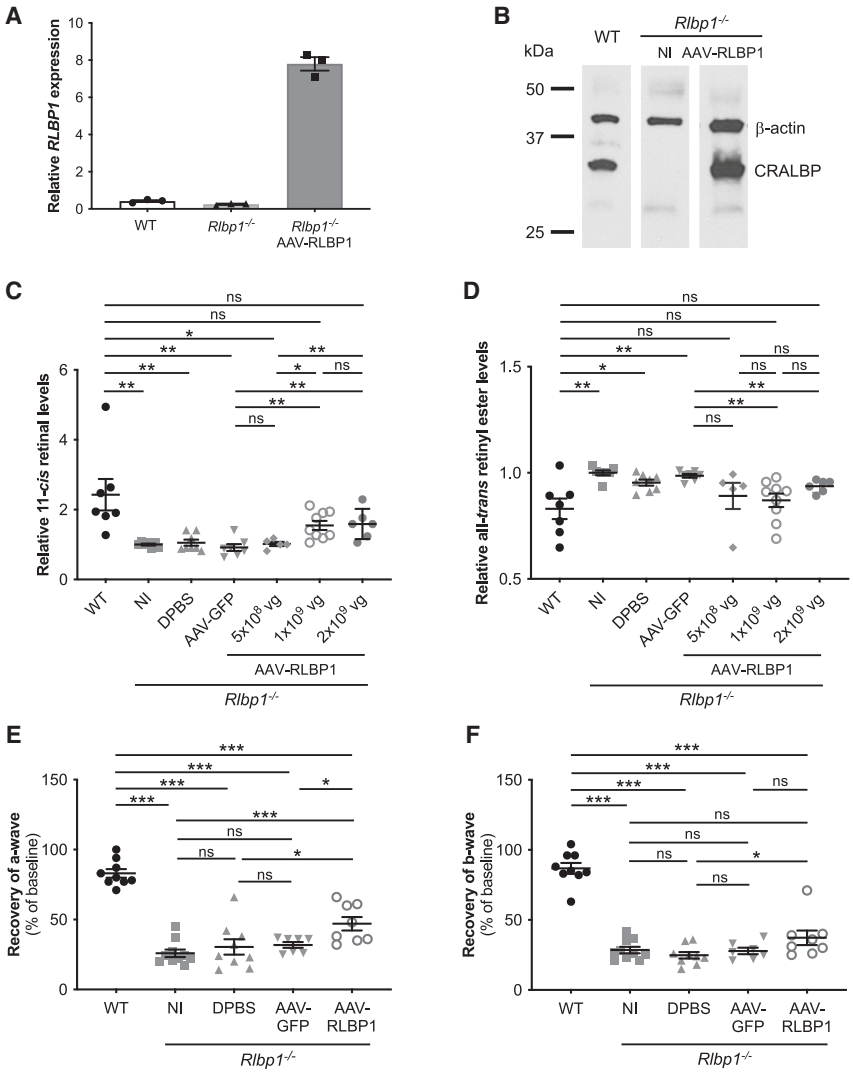

Figure 8. Rescue of visual cycle kinetics and retinal function in *Rlbp1*$^{-/-}$ mice

(A) qPCR analysis of human *RLBP1* in the eyes of wild-type (WT) and *Rlbp1*$^{-/-}$ mice non-injected (NI) or injected with 1 × 10^9 vg of the AAV-RLBP1 vector. Data are represented as mean ± SEM. (B) Representative western blot analysis of CRALBP in the eyes of WT and *Rlbp1*$^{-/-}$ mice NI or injected with AAV-RLBP1; β-actin represents the loading control. The mouse monoclonal anti-CRALBP antibody cross-reacted with murine CRALBP in the WT mouse. HPLC analysis of 11-*cis*-retinal (C) and all-*trans*-retinyl ester (D) levels in 4- to 6-month-old WT and *Rlbp1*$^{-/-}$ mice that were NI or injected with DPBS, AAV-GFP, or a low (5 × 10^8 vg), medium (1 × 10^9 vg), or high (2 × 10^9 vg) dose of AAV-RLBP1 up to 8 weeks post treatment. All data are represented as mean ± SEM and expressed relative to NI *Rlbp1*$^{-/-}$ mice; *$p < 0.05$; **$p < 0.01$; ns, non-significant; $n = 7$ (WT), 7 (NI), 8 (DPBS), 7 (AAV-GFP), 5 (AAV-RLBP1 5 × 10^8 vg), 9 (AAV-RLBP1 1 × 10^9 vg), and 6 (AAV-RLBP1 2 × 10^9 vg); Student's t test. Analysis of the recovery of a-wave (E) and b-wave (F) ERG amplitudes (as a percentage of baseline amplitudes) in 4- to 8-month-old WT and NI, DPBS-injected, AAV-GFP-injected, and AAV-RLBP1 (1 × 10^9 vg)-injected *Rlbp1*$^{-/-}$ mice up to 10 weeks post treatment. Data are represented as mean ± SEM; *$p < 0.05$; ***$p < 0.001$; ns, non-significant; $n = 9$ (WT), 10 (NI), 9 (DPBS), 7 (AAV-GFP), and 8 (AAV-RLBP1); Student's t test.

production, we selected the intermediate 1 × 10^9-vg dose for subsequent experiments.

To assess retinal function improvement in AAV-RLBP1-treated *Rlbp1*$^{-/-}$ mice, we conducted scotopic electroretinogram (ERG) recordings following light stimulation. Baseline ERG function was first evaluated in wild-type and non-, DPBS-, AAV-GFP-injected, and AAV-RLBP1-injected *Rlbp1*$^{-/-}$ mice up to 8 weeks after subretinal injection. All experimental groups exhibited similar a-wave (primarily from photoreceptors; Figure S4B) and b-wave (primarily from bipolar cells; Figure S4C) responses that decreased or increased, respectively, with increasing light intensity. Two weeks later, ERG recordings of the same animals were performed after photobleaching and dark adaptation (Figures S4D and S4E). To assess the recovery of retinal function, post-photobleaching values were expressed as a percentage of baseline values for each mouse and averaged by experimental group. Wild-type mice almost fully recovered their a-wave (Figure 8E) and b-wave (Figure 8F) amplitudes, whereas non-injected *Rlbp1*$^{-/-}$ mice did not. Similarly, there were no significant differences in recovery in DPBS- or AAV-GFP-injected *Rlbp1*$^{-/-}$ mice compared to non-injected mice. By contrast, AAV-RLBP1-injected *Rlbp1*$^{-/-}$ mice showed significant recovery of a-wave amplitudes compared to non-, DPBS-, and AAV-GFP-injected controls. Their b-wave amplitudes showed a trend toward improvement that was only statistically significant when compared to the DPBS-injected mice. Together, these findings suggest enhanced photoreceptor function in the AAV-RLBP1-treated group.

Taken together, treatment by AAV-RLBP1 improves visual cycle kinetics and outer retinal function in *Rlbp1*$^{-/-}$ mice, further validating this therapeutic vector in an animal model.

DISCUSSION

The advances made toward clinical gene-supplementation therapy for IRDs provided much optimism for both patient and scientific communities. Following the success of *RPE65* gene therapy, numerous clinical trials targeting various IRD genes,[34] including *RLBP1* in 2018 (NCT03374657), have been initiated. In this study, we report a proof of concept for *RLBP1*-supplementation therapy *ex vivo* in patient-specific iPSC-derived RPE models and *in vivo* in the murine knockout model. Our findings not only demonstrate phenotypic

and functional restoration in these models but also reveal that *RLBP1* expresses two CRALBP isoforms. Importantly, we provide direct evidence that these isoforms are differentially expressed both in human and murine retina and suggest that the smaller CRALBP isoform may be required for optimal visual cycle activity.

Western blot analysis of CRALBP has been extensively documented in various species (bovine,[35] murine,[36] human[37]) without report of a second isoform. For example, western blot analysis of HEK293 cells transfected with *RLBP1*-expressing plasmids clearly resulted in two CRALBP bands, but this finding was not discussed by the authors.[38] Similarly, analysis of human ARPE19 cells overexpressing MITF[39] also revealed two CRALBP bands that were not highlighted. Notably, a study on human donor RPE showed two CRALBP bands following western blot analysis of fresh RPE culture.[40] Although the authors did not comment on this, it corroborates our observations on human iPSC-derived RPE. Furthermore, Wenzel et al. analyzed CRALBP alongside the other retinal proteins RGR, RPE65, and RDH5 in murine eye cups and the CRALBP bands were clearly thicker.[41] This observation was understandably not emphasized but clearly resembles our findings on low-resolution gels where the two isoforms migrated close together. Thus, our study is the first report of a second CRALBP isoform.

Interestingly, a study of CRALBP in the visual cycle in zebrafish reported two bands on western blot analysis, contrasting with the expected single band in bovine and mouse eye.[42] It should be noted that the observed thickness of the bovine band, coupled to the conserved methionine codon at position 10 of bovine CRALBP, highly suggest the presence of two bovine isoforms. By contrast, the two zebrafish CRALBP bands were attributed to the identification of two ohnologues: *rlbp1a* predominant in the RPE, and *rlbp1b* in Müller glia. The Müller rlbp1b isoform is slightly smaller than the RPE rlbp1a isoform as it is missing the PDZ-domain target motif at the C terminus, suggesting distinct functional roles. This is notably different from our findings where both CRALBP isoforms contain the C-terminal PDZ-domain target motif but vary in the N terminus. Along this line, Crabb et al. described a doublet in recombinant human CRALBP protein on SDS-PAGE analysis that was attributed to a minor truncation of the first eight aa residues.[43] It was concluded that the truncation might be due to lability of the N-terminal region to proteolysis. We did perform an *in silico* study of the CRALBP protein sequence using the N-terminal protein translational modification prediction program Terminus (http://terminus.unige.ch/). The only notable prediction was an N-alpha acetylation and cleavage of the first five aa of CRALBP (MSEGV); however, no such truncated peptides were detected by mass spectrometry proteomic analysis.

The *in vitro* visual cycle assays conducted in this study did not provide definitive evidence regarding a role of the shorter CRALBP isoform in the visual cycle. Although this potential role needs to be examined by more extensive studies, it is worth noting that CRALBP has been reported to bind both 11-*cis*-retinol[44] and 11-*cis*-retinal.[45,46] If this is the case, then the two isoforms may bind these retinoids differentially. Interestingly, the small CRALBP isoform does not appear to play a role in Müller cells as it was not detected in human or murine neuroretina. Furthermore, the reported cooperation between RGR and CRALBP in both RPE and Müller glia,[19] and the fact that only 11-*cis*-retinal is produced in both cell types, further supports the rationale for the presence of both isoforms in RPE where 11-*cis*-retinol is also present.

Recent studies using conditional knockout models have provided additional insights into the role of CRALBP in the visual cycle. Specifically, one study reported conditional knockout mouse models of *Rlbp1*/CRALBP in the RPE (RPE-KO) or Müller glial cells (MG-KO).[47] The authors demonstrated that the RPE-KO mice recapitulate the phenotype of *Rlbp1*$^{-/-}$ mice (i.e., delayed rod dark adaptation, delayed visual chromophore regeneration, and retinyl ester accumulation). Furthermore, they showed that cone ERG responses were also suppressed in RPE-KO mice, whereas they were only mildly affected in MG-KO mice, and this was attributed to a disturbance of the RGR-based visual cycle. These data are consistent with findings in the conditional knockout models of the zebrafish ohnologues *rlbp1a* and *rlbp1b*.[48] Together, these studies reinforce the notion that the classic visual cycle in the RPE supports both rod and cone vision, whereas the Müller cycle plays a subsidiary role. Furthermore, they align with our data suggesting a specific need for both CRALBP isoforms in the RPE where CRALBP plays a dominant role. It is noteworthy that a CRALBP sequence alignment from 34 primate species showed that the second methionine codon, which produces the smaller isoform, is conserved in 31 species. Interestingly, the three primates that did not carry a methionine at position 10 are all nocturnal.

The phenotypes of the conditional knockout animal models also suggest that the RPE should be the major target when considering gene-supplementation strategies for *RLBP1*-associated IRDs.[47] Therefore, for therapeutic efficiency, it is crucial that the transgene cassette is capable of producing both CRALBP isoforms. Our AAV-RLBP1 vector successfully produced both isoforms, and their presence likely contributed to the success of the proof-of-concept studies in both patient-specific iPSC-derived RPE and murine *Rlbp1*$^{-/-}$ RPE. By comparison, only a single CRALBP band was detected by western blot analysis following subretinal delivery of the previously reported scAAV2/8-hRLBP1-RLBP1 vector,[24] which is currently being tested clinically. To rule out variables in sample preparation, we tested the same Cell Signalling buffer and protease inhibitors as those reported in that study in western blot analysis of our proviral plasmids, but we still detected two isoforms. It cannot be excluded that the single band observed in the scAAV2/8-hRLBP1-RLBP1 study was due to western blot migration conditions, as only a single CRALBP band was also detected in wild-type eyes.

An alternative explanation could lie with the different promoters used in the AAV2/5-CAG-RLBP1 and scAAV2/8-hRLBP1-RLBP1 vectors. Choi et al. used a short endogenous *RLBP1* promoter, which showed reduced *RLBP1* levels when compared to the long promoter in the

single-strand vector genome conformation but reached similar levels in the self-complementary conformation.[24] It could be hypothesized that the selected portion of the *RLBP1* promoter did not express high enough transcript levels, in contrast to the strong CAG promoter used in our study, for subsequent production of both CRALBP isoforms. Along this line, two parallel RPE65 clinical trials illustrated that expression levels may be related to efficiency. A trial using an AAV2/2 vector with *RPE65* under control of the CAG promoter[49] had more dramatic results than that using an RPE65 endogenous promoter,[50] suggesting that the lower response might be due to the use of the weaker promoter.[51] Perhaps more pertinent here, Kennedy et al. suggested that alternate promoter/elements might be required for CRALBP expression in Müller glia versus RPE, but these have not been identified to date.[52] It is thus conceivable that minimal regions of endogenous promoters may lack specific elements that could impact transcriptional regulation and the production of different protein isoforms. If our conclusions concerning the importance of the second isoform are correct, its absence in the scAAV2/8 vector could impact the efficiency of this vector relative to the newly reported AAV2/5 vector, raising important considerations for gene-supplementation therapy.

Another important aspect of our study is that, to our knowledge, we describe the first human iPSC-derived RPE models of *RLBP1*-associated IRDs and demonstrate salient genotype-phenotype correlations. We show that the iPSC-derived RPE from *RLBP1* patients expresses characteristic markers and remains tight in culture, similar to control RPE. The visual cycle defect emblematic of CRALBP deficiency was shown by increased all-*trans*-retinyl ester levels and retinosome accumulation, which correlated with clinical severity. Consistently, all-*trans*-retinyl ester accumulation has been reported in *Rlbp1*$^{-/-}$ mice[16,53] and lipid-droplet accumulation has been noted in the zebrafish knockout model of the RPE-specific ohnologue, *rlbp1a*.[48] Furthermore, it was suggested that these lipid droplets were reminiscent of the subretinal white lesions characteristic of *RLBP1* patients.

A comparative study demonstrated that *RLBP1* patients show similar ERG profiles and chronic impairment in 11-*cis*-retinal availability as *Rlbp1*$^{-/-}$ mice.[53] Furthermore, the 11-*cis*-retinal deficiency resulted in measurably reduced autofluorescence, which was age-related in mice and related to mutation severity in humans. The characteristic white lesions in patients indicated RPE changes that progress to atrophy, with structural changes in the photoreceptor layer consistent with photoreceptor degeneration observed in aged *Rlbp1*$^{-/-}$ mice. Consistently, we identified altered iPSC-derived RPE functionality, which would contribute to reduced photoreceptor health, that was more evident in the RPE from patient RPA3, who presented with the severe NFRCD. As MERTK expression seemed intact, we speculate that the altered phagocytic activity, as well as growth factor secretion, were not primary defects but likely consequences of the subcellular changes due to retinosome accumulation.

CRALBP localization in iPSC-derived RPE also varied depending on the *RLBP1* variant/clinical form. In control iPSC-derived RPE, CRALBP exhibits dual subcellular profiles. It is tempting to speculate that the cytosolic localization could be related to 11-*cis*-retinol binding following photoisomerization, while the membrane localization could be linked to the transfer of the 11-*cis*-retinal to IRBP at the plasma membrane. These localization profiles align with prior studies in mouse and rat RPE.[54] Interestingly, in the RPE of patient RPA1 (BD), the plasma membrane localization was lost and CRALBP appeared more cytosolic. This finding is reminiscent of our previous observations in an iPSC-derived RPE model of another IRD caused by TBC1D32 deficiency, which also showed a disruption of the visual cycle.[28] By contrast, the RPE of patient RPA2 (RPA), who presented with the mildest clinical form, preserved the dual CRALBP localization pattern, although CRALBP staining was less intense. No CRALBP, irrespective of isoform, was detected in RPA3, consistent with the severe NFRCD phenotype.

Both RPA1 and RPA2 RPE harbor a nonsense variant, p.Tyr111*, in combination with a missense variant, which we previously modeled.[6] The reduced *RLBP1* levels in the RPE of these patients strongly suggest that the p.Tyr111* variant does not result in CRALBP expression. In RPA2 RPE, we observed clear expression of two CRALBP isoforms by western blot analysis. Therefore, we hypothesize that the pArg9Cys variant carried by RPA2, located immediately upstream of the second initiation codon, may allow the production of a mutant larger isoform but also an intact smaller isoform. This would account for the milder phenotype in this patient. This aligns with the *in vitro* visual cycle assay showing that the presence of the smaller isoform alone does not result in significantly decreased 11-*cis*-retinol levels. By contrast, in RPA1 RPE, both CRALBP isoforms would carry the p.Arg234Trp mutant, consistent with the more severe clinical phenotype. The crystal structure of CRALBP-p.Arg234Trp suggests that the mutant protein(s) has tighter binding to 11-*cis*-retinal,[55] leading to increased resistance to light-induced photoisomerization.[56] Interestingly, we detected the smaller CRALBP isoform less readily by western blot analysis in RPA1 RPE. If we correlate this observation with the IF data showing the loss of CRALBP near the plasma membrane, it could suggest that the smaller isoform is associated with the membrane and, hence, as speculated above, is involved in 11-*cis*-retinal binding and transfer to IRBP for entry to the POS.

Taken together, further study of both control and patient-specific iPSC-derived RPE may provide valuable insights into CRALBP function and the roles of the canonical and non-canonical isoforms in the visual cycle. Meanwhile, modeling *RLBP1*-associated IRDs using iPSC-derived models has enabled us to identify quantitative criteria for evaluating the efficacy of *RLBP1* gene supplementation in human RPE, which was consolidated by our murine proof-of-concept study. Consequently, these models will also be invaluable for evaluating other emerging therapies for *RLBP1*-associated IRDs.

MATERIALS AND METHODS

Clinical examinations and iPSC generation

Color fundus photography was performed using an automated, nonmydriatic fundus camera (AFC 330, Nidek). Dermal fibroblasts were

cultured from skin biopsies and reprogrammed under feeder-free conditions using the integration-free CytoTune iPSC 2.0 Sendai Reprogramming kit.[26] iPSCs were cultured on dishes coated with 1:100 dilution of Matrigel human embryonic stem cell (hESC)-qualified matrix (Corning) in Essential 8 (E8) medium (Gibco) and passaged weekly using 0.48 mM Versene solution (Gibco). For karyotype analyses, iPSCs were prepared as described[26] and 20 metaphase spreads were analyzed using standard G-banding techniques (Chromostem facility, Montpellier University Hospital, France). For the teratoma assay, a confluent non-differentiated 35-cm^2 dish of iPSCs was dissociated with Versene, centrifuged for 5 min at 800 rpm, resuspended in E8 medium containing 30% Matrigel, and injected into NOD.Cg-Prkdc^{scid}/J mice.[25] Paraffin-embedded 4-μm sections were stained with hematoxylin-eosin-saffron using standard protocols and images taken using an upright Eclipse Ci-L plus microscope connected to a DS-Fi3 digital microscope camera and NIS-Elements L Imaging software (Nikon).

iPSC-derived retinal differentiation

iPSCs were spontaneously differentiated into RPE and cultured in KnockOut DMEM medium (Gibco) supplemented with 20% KnockOut Serum Replacement (KOSR; Gibco), 1% GlutaMax (Gibco), 1% non-essential aa (Gibco), 0.1% β-mercaptoethanol, and 1% penicillin-streptomycin.[26] At passage (P) 3, RPE was seeded at a density of 6×10^4 cells per 0.32 cm^2 on a 1:30 dilution of Corning Matrigel hESC-qualified matrix on cell culture inserts with high-density 0.4-μm pores (Falcon), 24-well plates, or 6-well plates depending on the experiment. TER measurements were performed as described without modification.[26] iPSCs were differentiated into retinal organoids using a 2D-3D differentiation protocol supplemented with retinoic acid.[57]

Phagocytosis and growth factor secretion

Bovine POS were prepared as described.[58] iPSC-derived RPE cultured on membrane inserts were fed with 7.5 POS/cell for 2.5 h at 37°C, washed, dissociated with 0.25% trypsin, and pelleted. Cells were resuspended in 200 μL of PBS and fluorescence analyzed on a BD Accuri C6 Flow Cytomoter (BD Biosciences). VEGF and PEDF levels were assayed by ELISA (R&D systems) on 24-h conditioned media collected from the apical and basolateral chambers of 4-month-old iPSC-derived RPE cultured on inserts.[32] Optical densities were determined at 450 nm using a microtiter plate reader (Clariostar; BMG Labtech). Samples were collected from nine inserts per condition, assayed in triplicate, and the mean expressed as percentage of control values.

TEM and multiphoton microscopy

Three- to 7-month-old iPSC-derived RPE cultured on inserts was processed and embedded for TEM analysis as described.[26] Counterstained 70-nm sections were observed using a Tecnai F20 transmission electron microscope at 200 kV (CoMET facility, INM). Lipid droplets were counted manually and counting confirmed by an additional masked investigator. Fixed 7-month-old iPSC-derived RPE cultured on inserts was imaged using a Zeiss LSM 880 multiphoton associated with an Upright AxioExaminer microscope and equipped with a Ti:sapphire femtosecond laser (Chameleon Ultra II; Coherent France). Stimulation was performed at a wavelength of 740 nm and emission was recorded between 500 and 550 nm. Images were treated using the Imaris IsoSurface module (Oxford Instruments). The area of fluorescence was calculated relative to the area of each image.

AAV proviral plasmid and vector generation

The *RLBP1* cDNA (NM_000326) from the ATG (+1) to the TGA codon (kindly provided by John Crabb, Cleveland Clinic Foundation) was PCR amplified using AmpliTaq Gold DNA polymerase (Applied Biosystems) with the forward (F) *Mlu*I-containing primer and the reverse (R) *Xho*I-containing primer (see Table S1) under standard conditions. The 966-bp amplicon was purified using the Wizard SV Gel and PCR Clean-Up System (Promega) and subcloned into the TA cloning vector pGEM-T easy (Promega) according to the manufacturers' recommendations. DNA was isolated from *RLBP1*-containing pGEM-T easy colonies and digested with *Mlu*I and *Xho*I (Promega) for 3 h at 37°C. The excised *RLBP1* insert was gel purified using the Mini Elute Gel Extraction kit (Qiagen) and ligated using T4 DNA ligase (Promega) at room temperature (RT) for 1 h into the *Mlu*I/*Xho*I-digested recombinant AAV proviral plasmids pDDO-020-SSV9-CAG-bGHpA or pKL-AAV-CAG-bGHpA (provided by the TaRGet vector core, Nantes, France). Five microliters of the ligation reaction were transformed into MAX Efficiency Stbl2 Competent Cells (Invitrogen) and cultured at 30°C to minimize recombination between the ITRs. Resulting clones were screened by restriction enzyme digestion to assay for ITR stability and correct *RLBP1* insertion. Positive pDDO-RLBP1 or pKL-RLBP1 clones were verified by Sanger sequencing with an F primer in exon 5 and an R primer spanning the junction of exons 7 and 8. DNA from the selected clone was purified using the EndoFree Plasmid kit (Promega) and sent to the TaRGet vector core to generate the corresponding AAV-RLBP1 vector (production titers: 1.2×10^{12} vg/mL for the pDDO batch and 3.3×10^{12} vg/mL for the pKL).

PCR analysis and Sanger sequencing

Plasmid DNA was isolated using the Qiaprep Spin Miniprep Kit (Qiagen) and genomic DNA using the DNeasy Blood and Tissue Kit (Qiagen). The exons containing the *RLBP1* variants carried by the patients RPA1 and RPA2 in exons 4, 5, and 8 were PCR amplified using the primers listed in Table S1. Amplicons were cleaned with the ExoSAP-IT PCR clean-up kit (GE Healthcare) and Sanger sequencing was carried out using the BigDye Terminator Cycle Sequencing Ready Reaction kit V3.1 on a 3130xL Genetic Analyzer (Applied Biosystems, Foster City, CA). A total of 50 ng of amplified genomic DNA or 250 ng of plasmid DNA and 3.2 μM primer were used for each reaction. Reactions were precipitated and resuspended in 15 μL of ultrapure formamide before sequencing. To assay for the large deletion carried by patient RPA3, long-range PCR was performed using the TaKaRa Taq DNA polymerase and an F primer in intron 6 of *RLBP1* and an R primer situated in the intergenic region between *RLBP1* and *ABHD2* gene (Table S1).[3] Amplicons were migrated on a 1% agarose gel.

Transfections

COS-7 and HEK293 cells were plated at a density of 4×10^4 cells/cm^2 or 1×10^5 cells/cm^2, respectively, in 24-well plates for qPCR or western blot analyses, on glass coverslips in 24-well plates for IF studies, in 12-well plates for western blot analysis, or in 6-well plates for retinoid assays. Cells were cultured in DMEM medium supplemented with 10% FBS (Gibco) for 24 h prior to transfection. Experimental wells were transfected with 500 ng (24-well plates), 1 μg (12-well plates), or 2.5 μg (6-well plates) of plasmid DNA diluted in OptiMEM medium using the Lipofectamine 3000 reagent (Invitrogen, Thermo Fisher Scientific, France) for 48 h. As a control condition, non-transfected cells were incubated with the transfection reagents in Opti-MEM medium without plasmid DNA. For all experiments, transfections were performed in duplicate.

Proteomic analysis

Transfected COS-7 cells were scraped in ice-cold PBS containing Complete protein inhibitor cocktail tablets (Roche), centrifuged at $200 \times g$ for 5 min, and the pellet was lysed in radioimmunoprecipitation assay (RIPA) buffer (5 M NaCl, 0.5 M EDTA pH 8, 1 M Tris pH 8, 10% sodium deoxycholate, 10% SDS) under agitation at 4°C for 30 min. The lysate was cleared by centrifugation at $21{,}130 \times g$ at 4°C for 30 min and protein content quantified using the Pierce BCA protein assay kit (Thermo Fisher Scientific). Twenty micrograms of cell lysate, 2.5 μg of recombinant His-tagged CRALBP protein (ab177594, Abcam), and a SeeBlue Prestained Protein marker (LC59225, Thermo Fisher Scientific) were loaded on two 12% precast gels (Life Technologies system). Following electrophoresis, one gel was transferred onto a polyvinylidene fluoride (PVDF) membrane and hybridized with the mouse monoclonal anti-CRALBP antibody. The second gel was rinsed and stained in Coomassie blue staining solution (InstantBlue, Expedeon) for 1 h. The bands of interest were cut from the Coomassie-stained gel using the western blot filter as a guide and an in-gel digestion using a protease (sequencing grade trypsin, Promega) was performed prior to proteomic analysis by nanoscale liquid chromatography coupled to tandem mass spectrometry (nano LC-MS/MS) using a QTOF Impact II (Bruker Daltonics) mass spectrometer, as described.[59]

Site-directed mutagenesis

The ATG (+1) codon of pKL-RLBP1 was mutated to an alanine codon (GCG) using the QuikChange Site-directed Mutagenesis kit (Agilent technologies) with the F primer and its reverse complement (Table S1) to generate pKL-RLBP1-Met1Ala. The ATG (+10) codon of pKL-RLBP1 was mutated to a GCG codon using the Assembly PCR oligo maker.[60] A first round of amplification was performed for eight cycles using a mix of six overlapping primers (Table S1) spanning the first five *RLBP1* exons (primer F1 flanked the ATG [+1] codon and R2 contained the mutated ATG). A second round of amplification was performed for 25 cycles using primers flanking the ATG codon (22 bp upstream and 200 bp downstream). The purified amplicon was digested by *Mlu*I and *Bsa*I and subcloned into *Mlu*I/*Bsa*I-digested pKL-RLBP1 to generate pKL-RLBP1-Met10Ala. Following mutagenesis and/or subcloning, both ATG-mutated plasmids were transformed into MAX Efficiency Stbl2 Competent Cells (Invitrogen). Clones were screened by restriction enzyme digestion and verified by Sanger sequencing using F primers in the pKL backbone upstream of *RLBP1* and in exons 5 and 7 of *RLBP1*, and R primers in exons 5 and 6 of *RLBP1* (Table S1), to cover the entire open reading frame. Prior to the generation of the c.700C>T (p.R234W) and c.25C>T (p.R9C) mutagenesis plasmids, the *RLBP1* cDNA was removed by *Mlu*I/*Xho*I digestion of pKL-RLBP1 and subcloned into pGEM-T easy to avoid unwanted recombination events due to the repetitive ITR sequences. Mutagenesis was performed using the primers listed in Table S1 and verified by Sanger sequencing. The mutant cDNAs were subcloned back into the pKL plasmid to generate pKL-RLBP1-Arg9Cys and -Arg234Trp.

Reverse transcription and qPCR analyses

Transfected COS-7 cells and iPSC-derived RPE were dissociated with 0.25% trypsin (Gibco), and iPSCs with Versene, centrifuged, and snap-frozen in liquid nitrogen. Following sacrifice, wild-type and untreated and treated *Rlbp1*$^{-/-}$ mouse eyes were enucleated, the anterior segment and the lens were removed, the neuroretina dissected, and the remaining RPE scraped and collected. The neuroretina and RPE were pooled and snap-frozen. RNA from transfected cells, iPSCs, iPSC-derived RPE, and murine tissues were isolated using the QiaShredder and RNeasy mini kits (Qiagen, France). The isolated RNA was treated with RNase-Free DNase (Qiagen) and 150 or 500 ng (for iPSCs) was reverse transcribed using the Superscript III Reverse Transcriptase kit (Life Technologies, Thermo Fisher Scientific). Clearance of the Sendai vectors was assayed by RT-PCR amplification of fibroblast and iPSC cDNA with primers specific to the vector backbone (SEV), polycistronic cassette (KOS), and monocistronic cassettes (KLF4, c-MYC) (Table S2). qPCR amplification of a 1:10 dilution of cDNA was performed in triplicate on a LightCycler 480 II thermal cycler (Roche, France) using the LightCycler 480 SYBR Green I Master mix and specific primers (Table S2). Results were analyzed using LightCycler 480 software and the Microsoft Excel program Quantification was performed using the ΔΔCt method, normalized to *GAPDH* for human cells and *L27* for murine tissues, and expressed relative to control.

Western blot analysis

Non-transfected and transfected COS-7 and HEK293 cells, non-transduced and transduced iPSC-derived RPE, and organoids were scraped or collected in ice-cold PBS containing Complete protein inhibitor cocktail tablets (Roche) (unless otherwise stated) and centrifuged at $200 \times g$ for 5 min. Pellets were resuspended in 30 μL of 2× Laemmli sample buffer (Bio-Rad, France) containing 1:25 dilution of β-mercaptoethanol (Sigma-Aldrich) and 1 μL of Benzonase (Sigma-Aldrich) or in RIPA buffer (unless otherwise stated) and centrifuged at $20{,}000 \times g$ for 15 min prior to protein quantification using the Pierce BCA protein assay. iPSC-derived organoids and dissected neuroretina and RPE from wild-type and *Rlbp1*$^{-/-}$ mice were lysed in 30 μL of RIPA buffer using a mortar and pestle, centrifuged at $20{,}000 \times g$ for 15 min, and the proteins were quantified prior to loading (murine tissues) or directly loaded (organoids). Samples

(25 μL total volume) were heated 5 min at 95°C and loaded onto an AnykD precast MiniProtean TGX Stain Free gel (Bio-Rad) or a 15% SDS-PAGE gel, as specified. The separated proteins were electrotransferred using a Trans-Blot Turbo Mini PVDF Transfer Pack and System (Bio-Rad). After blocking for 1 h in 0.5% Tween-PBS in 5% skim milk (blocking solution), membranes were incubated with primary antibodies (Table S3) overnight at 4°C, washed in 0.5% Tween-PBS, and with secondary antibodies (Table S4) for 45 min at RT. The detection step was performed using the Amersham ECL prime western blotting detection reagent (GE Healthcare, France) and visualized using autoradiographic film exposure and a Bio-Rad ChemiDoc XRS+ Imager system or using an Odyssey CLx Imager (Li-COR Biosciences) and quantified with the Image Studio Lite or Empiria Studio software. β-Actin was used as the loading control in all experiments.

IF studies

Uncoated or poly-D-lysine-coated (HEK293) glass coverslips containing non-transfected and transfected COS-7 and HEK293 cells, respectively, and inserts containing iPSC-derived RPE were fixed in 4% paraformaldehyde (PFA; Alfa Aesar) for 10 min at RT, blocked in 10% donkey serum (Millipore) and 1% BSA (Sigma-Aldrich) in PBS, and permeabilized with 0.3% Triton X-100 (Sigma-Aldrich). Retinal organoids were washed in PBS, fixed in 4% PFA, incubated in 30% sucrose/PBS overnight at 4°C, and embedded in Tissue-Tek OCT compound (Sakura). Slides with 10-μm cryosections were incubated in 10% donkey serum, 5% BSA, and 0.1%Triton X-100 for 1 h at RT. For all cell types, primary antibodies (Table S3) were incubated overnight at 4°C and secondary antibodies (Table S4) with 0.2 mg/mL bisBenzimide (Hoechst; Sigma-Aldrich) or 1 μg/mL DAPI (Sigma-Aldrich) were incubated for 45 min at RT prior to mounting in Dako Fluorescent Mounting Media (Dako France SAS, Les Ulis, France). Cells were visualized using an ApoTome 2 Upright wide-field or a Confocal LSM 880 microscope (Carl Zeiss SAS).

Visual cycle experiments

HEK293 cells stably expressing human LRAT[33] were transfected with plasmids carrying control *RPE65*[33] and *RLBP1* sequences or the mutated Met1Ala and Met10Ala *RLBP1* sequences. Under dim light, transfected HEK293 cells were starved in serum-free medium for 8 h and incubated for 24 h in KnockOut DMEM, 15% KOSR, 2% fatty acid-free BSA (Sigma), and 10 μM vitamin A (Sigma, R7632). Human iPSC-derived RPE aged 6 to 8 weeks was starved in RPE medium without KOSR for 8 h and incubated for 24 h. After 8 h, the media was changed to RPE medium without KOSR supplemented with 2% fatty acid-free BSA, 15% FBS (Gibco) and 10 μM vitamin A.[61] All cells were scraped in PBS, pelleted, and stored in the dark at −80°C. HEK293 and RPE pellets were lysed in 200 μL of 0.2% SDS/PBS. Ten microliters was withdrawn for protein quantification using the Pierce BCA protein assay (Thermo Fisher) and 300 mL ethanol and 1 mL of hexane were added to the remainder of the lysate, which was then processed for HPLC analysis, as described below. Three independent experiments were performed.

AAV transduction

Ten to 12 weeks post seeding, iPSC-derived RPE was transduced with 50,000 vg/cell of AAV-RLBP1 in 100 μL (inserts) or 200 μL (24-well plates) of medium for 6 h. The wells were then supplemented with 100 μL (inserts) or 200 μL (24-well plates) of medium overnight and another 100 μL or 500 μL, respectively, the next morning. The medium was refreshed 2 days post transduction and the transduced RPE was kept in culture for 8 weeks.

Rlbp1$^{-/-}$ mouse colony

The *Rlbp1*$^{-/-}$ mouse model[16] of mixed 129/SvJ, C57BL/6J, and BALB/c backgrounds was kindly provided by the Cleveland Clinic (Beachwood, OH, USA). The founders were crossed with C57BL/6J mice (Harlan France SARL, Gannat, France) and the colony maintained in a controlled environment with a 12-/12-h light/dark cycle according to the European guidelines for the care and use of laboratory animals (EU directive 2010/63/EU). The colony was homozygous for the p.Leu450Met variant of RPE65.[36] For genotyping, genomic DNA was extracted and the *Rlbp1* alleles were amplified using the Phire Tissue Direct PCR master mix (Thermo Fisher Scientific) and a forward primer in combination with two reverse primers (Table S1) to distinguish between the wild-type and *Rlbp1*$^{-/-}$ alleles.[16]

Subretinal injection

Adult mice were anesthetized with ketamine (70 mg/kg; Merial, France) and xylazine (28 mg/kg; Bayer Healthcare, France) systemically and 0.4% oxybuprocaine (Cebesine, Bausch + Lomb, France) locally. The pupils were dilated by the sequential administration of a drop of 10% phenylephrine (Neosynephrine, Europhta) and 0.5% tropicamide (Mydriaticum, Théa, France), and the cornea was covered with a drop of Lacryvisc (Alcon, France) and a glass coverslip. Under a surgical microscope, the eye was first pierced at the corneal-scleral junction to relieve intra-ocular pressure. Subsequently, subretinal injections were performed using a 5-μL Hamilton syringe and a beveled 34G needle. On the experimental day, the AAV-RLBP1 vector was diluted in DPBS to the required dose and a maximum of 2 μL was injected into one eye of an *Rlbp1*$^{-/-}$ mouse. The contralateral eye was either left non-injected or injected with 2 μL of DPBS or an AAV-GFP vector to control for the surgical procedure and non-specific effects of the AAV vector, respectively. Following injection, the needle was slowly removed to avoid any reflux. If a subretinal bleb did not form upon injection or was lost upon removal of the needle, or if a second injection was performed, the eye was excluded from the analysis. It should be noted that the bleb resulting from single-administration subretinal injection only covered between 20% and 50% of the retina. At the required time post injection, animals were euthanized by cervical dislocation.

HPLC

Mice were injected between 2 and 4 months of age. Eight-weeks post injection, the experimental groups were photobleached at 6,000 lux for 20 min and then dark adapted for 4 h. The animals were then euthanized and the ocular globe rapidly enucleated. The eyes were

homogenized in 300 µL of 3 M formaldehyde (Sigma), incubated at 30°C for 5 min, and supplemented with 0.3 mL of ethanol.[62] One milliliter of hexane (Sigma) was then added, the samples homogenized, and the organic phase collected. This step was repeated. The samples were then concentrated to 20 µL using a Speed Vac vacuum concentrator. Analyses were performed using a Varian HPLC system equipped with a NUCLEODUR SiOH column (4.6 × 250 mm) (Macherey-Nagel) and a Prostar 330 diode array detector. The elution was performed with 6% ethyl acetate in hexane for 10 min at a flow rate of 2 mL/min. The retinoids were quantified from the peak areas using calibration curves determined with established standards.

Electroretinogram recordings

Mice were injected between 2 and 6 months of age. All ERG recordings were performed following overnight dark adaptation, at the same time of the day, under dim red light in a dark room, and using the Visiosystem (SIEM, France) with cotton-wick electrodes.[63] Each animal was anesthetized, its pupils dilated, and kept on a heating pad throughout the experiment maintaining the rectal temperature at 37°C (Temperature Control Unit HB 101/2; Bioseb, France). A ground needle electrode was placed subcutaneously near the tail, and two reference electrodes were placed near the ears. ERG responses were recorded simultaneously from both eyes. The responses to seven flashes were averaged for each light intensity (−1, −0.7, −0.3, 0, 0.7, 1, 1.5, and 2 log candela second/m2 [cd.s.m^{-}2]). The duration of each flash was 5 ms with a frequency of 0.3 Hz. Baseline retinal function of the mice in all experimental groups was measured 2 weeks prior to photobleaching. Two weeks later, the same mice were dark adapted overnight, their pupils dilated, and photobleached by exposure to 2,000 lux for 5 min. Following illumination, mice were again dark adapted for 4 h prior to ERG recordings. The percentage of recovery was determined as the ERG recording post illumination over the baseline recording per eye. The values at a flash intensity of 1.5 cd.s.m^{-2} were used to generate the dot plots as the recordings were high but had not plateaued.

Statistical analyses

For groups of data that were predominantly normally distributed (Shapiro-Wilk test), 2 × 2 analysis was performed using a two-tailed Student's t test. For groups of data that were not normally distributed, 2 × 2 analysis was performed using a two-tailed Mann-Whitney test. Data were analyzed using GraphPad Prism 10 software (GraphPad Software, La Jolla, CA, USA). A p value <0.05 was considered significant. The number of samples per experiment and condition and the statistical test used are indicated in the corresponding figures or legends.

Study approval

Clinical and genetic investigations were performed following signed informed consent in accordance with protocols approved by the Montpellier University Hospital review board (ID no.: IRB-MTP_2021_11_202100959) and in agreement with the Declaration of Helsinki. Skin biopsies and iPSC reprogramming were performed following ethics approval by the local institutional review board and the French National Agency for the Safety of Medicines and Health Products (ID no.: 2014-A00549-38). Animal care and experimentation were approved by local and national review boards under the project number APAFIS#1192-2015071713533208.

DATA AND CODE AVAILABILITY

All data are available in the main text or the supplementary materials.

ACKNOWLEDGMENTS

We dedicate this work to Pr. Christian Hamel who helped initiate the study and passed away prematurely in 2017. We thank A. Conscience, M. Cavalier, A. Jemi, Z. Jazouli, K. Bellouma, C. Martin, and T. Duncan for technical assistance, and A.F. Roux for critical reading of the manuscript. We also thank C. Cazevieille of the CoMET facility (INM), P. Clair of the qPHD facility (University of Montpellier), the MRI imaging facility, and the RAM-Neuro animal facility. We particularly thank S. Marconi and N. Delauney (formerly of Horama) for stimulating scientific discussions. We are grateful to the individuals who participated in the study. This work was funded by Retina France, AFM-Telethon (grant no.: 16599), Fondation de France (grant no.: 00012185), and Fondation pour la Recherche Médicale (grant no.: VL/DLS/GP/vk111114). Part of the work was funded as a maturation project by the axLR SATT and a collaboration contract with Horama (now Coave Therapeutics and EyeDNA).

AUTHOR CONTRIBUTIONS

Co-first authors were assigned by order of arrival on the project. K.D., G.D., L.G., D.M., M.P., N.E., C.S.-S., F.B., and J.V. performed experiments. B.B. and I.M. provided genetic and clinical data. H.B. and C.H. analyzed data. T.M.R. and Y.A. shared expertise. P.B. and V.K. provided supervision and analyzed results. V.K. provided funding and wrote the manuscript. All authors reviewed and edited the manuscript.

DECLARATION OF INTERESTS

V.K. is scientific co-founder of Horama (now Coave Therapeutics and eyeDNA Therapeutics). V.K. and M.P. are inventors of the patent WO/2015/082690 concerning AAV-mediated gene transfer into the RPE.

SUPPLEMENTAL INFORMATION

Supplemental information can be found online at https://doi.org/10.1016/j.ymthe.2024.10.004.

REFERENCES

1. Grossniklaus, H.E., Geisert, E.E., and Nickerson, J.M. (2015). Introduction to the Retina. Prog. Mol. Biol. Transl. Sci. *134*, 383–396. https://doi.org/10.1016/bs.pmbts.2015.06.001.

2. Berger, W., Kloeckener-Gruissem, B., and Neidhardt, J. (2010). The molecular basis of human retinal and vitreoretinal diseases. Prog. Retin. Eye Res. *29*, 335–375. https://doi.org/10.1016/j.preteyeres.2010.03.004.

3. Humbert, G., Delettre, C., Sénéchal, A., Bazalgette, C., Barakat, A., Bazalgette, C., Arnaud, B., Lenaers, G., and Hamel, C.P. (2006). Homozygous deletion related to Alu repeats in RLBP1 causes retinitis punctata albescens. Invest. Ophthalmol. Vis. Sci. *47*, 4719–4724. https://doi.org/10.1167/iovs.05-1488.

4. Maw, M.A., Kennedy, B., Knight, A., Bridges, R., Roth, K.E., Mani, E.J., Mukkadan, J.K., Nancarrow, D., Crabb, J.W., and Denton, M.J. (1997). Mutation of the gene encoding cellular retinaldehyde-binding protein in autosomal recessive retinitis pigmentosa. Nat. Genet. *17*, 198–200. https://doi.org/10.1038/ng1097-198.

5. Morimura, H., Berson, E.L., and Dryja, T.P. (1999). Recessive mutations in the RLBP1 gene encoding cellular retinaldehyde-binding protein in a form of retinitis punctata albescens. Invest Ophthalmol. Vis. Sci. *40*, 1000–1004. https://doi.org/10.1038/70496.

6. Bocquet, B., El Alami Trebki, H., Roux, A.F., Labesse, G., Brabet, P., Arndt, C., Zanlonghi, X., Defoort-Dhellemmes, S., Hamroun, D., Boulicot-Séguin, C., et al. (2021). Retinitis Punctata Albescens and *RLBP1*-Allied Phenotypes: Phenotype-Genotype Correlation and Natural History in the Aim of Gene Therapy. Ophthalmol. Sci. *1*, 100052. https://doi.org/10.1016/j.xops.2021.100052.

7. Burstedt, M.S., Forsman-Semb, K., Golovleva, I., Janunger, T., Wachtmeister, L., and Sandgren, O. (2001). Ocular phenotype of bothnia dystrophy, an autosomal recessive retinitis pigmentosa associated with an R234W mutation in the RLBP1 gene. Arch. Ophthalmol. *119*, 260–267.

8. Burstedt, M.S., Sandgren, O., Holmgren, G., and Forsman-Semb, K. (1999). Bothnia dystrophy caused by mutations in the cellular retinaldehyde-binding protein gene (RLBP1) on chromosome 15q26. Invest. Ophthalmol. Vis. Sci. *40*, 995–1000.

9. Eichers, E.R., Green, J.S., Stockton, D.W., Jackman, C.S., Whelan, J., McNamara, J.A., Johnson, G.J., Lupski, J.R., and Katsanis, N. (2002). Newfoundland rod-cone dystrophy, an early-onset retinal dystrophy, is caused by splice-junction mutations in RLBP1. Am. J. Hum. Genet. *70*, 955–964. https://doi.org/10.1086/339688.

10. Katsanis, N., Shroyer, N.F., Lewis, R.A., Cavender, J.C., Al-Rajhi, A.A., Jabak, M., and Lupski, J.R. (2001). Fundus albipunctatus and retinitis punctata albescens in a pedigree with an R150Q mutation in RLBP1. Clin. Genet. *59*, 424–429. https://doi.org/10.1034/j.1399-0004.2001.590607.x.

11. Saari, J.C. (2000). Biochemistry of visual pigment regeneration: the Friedenwald lecture. Invest. Ophthalmol. Vis. Sci. *41*, 337–348.

12. Palczewski, K., and Kiser, P.D. (2020). Shedding new light on the generation of the visual chromophore. Proc. Natl. Acad. Sci. USA *117*, 19629–19638. https://doi.org/10.1073/pnas.2008211117.

13. Jin, M., Li, S., Moghrabi, W.N., Sun, H., and Travis, G.H. (2005). Rpe65 is the retinoid isomerase in bovine retinal pigment epithelium. Cell *122*, 449–459. https://doi.org/10.1016/j.cell.2005.06.042.

14. Moiseyev, G., Chen, Y., Takahashi, Y., Wu, B.X., and Ma, J.X. (2005). RPE65 is the isomerohydrolase in the retinoid visual cycle. Proc. Natl. Acad. Sci. USA *102*, 12413–12418. https://doi.org/10.1073/pnas.0503460102.

15. Redmond, T.M., Poliakov, E., Yu, S., Tsai, J.Y., Lu, Z., and Gentleman, S. (2005). Mutation of key residues of RPE65 abolishes its enzymatic role as isomerohydrolase in the visual cycle. Proc. Natl. Acad. Sci. USA *102*, 13658–13663. https://doi.org/10.1073/pnas.0504167102.

16. Saari, J.C., Nawrot, M., Kennedy, B.N., Garwin, G.G., Hurley, J.B., Huang, J., Possin, D.E., and Crabb, J.W. (2001). Visual cycle impairment in cellular retinaldehyde binding protein (CRALBP) knockout mice results in delayed dark adaptation. Neuron *29*, 739–748. https://doi.org/10.1016/s0896-6273(01)00248-3.

17. Mata, N.L., Radu, R.A., Clemmons, R.C., and Travis, G.H. (2002). Isomerization and oxidation of vitamin a in cone-dominant retinas: a novel pathway for visual-pigment regeneration in daylight. Neuron *36*, 69–80. https://doi.org/10.1016/s0896-6273(02)00912-1.

18. Wang, J.S., Estevez, M.E., Cornwall, M.C., and Kefalov, V.J. (2009). Intra-retinal visual cycle required for rapid and complete cone dark adaptation. Nat. Neurosci. *12*, 295–302. https://doi.org/10.1038/nn.2258.

19. Tworak, A., Kolesnikov, A.V., Hong, J.D., Choi, E.H., Luu, J.C., Palczewska, G., Dong, Z., Lewandowski, D., Brooks, M.J., Campello, L., et al. (2023). Rapid RGR-dependent visual pigment recycling is mediated by the RPE and specialized Muller glia. Cell Rep. *42*, 112982. https://doi.org/10.1016/j.celrep.2023.112982.

20. Xue, Y., Shen, S.Q., Jui, J., Rupp, A.C., Byrne, L.C., Hattar, S., Flannery, J.G., Corbo, J.C., and Kefalov, V.J. (2015). CRALBP supports the mammalian retinal visual cycle and cone vision. J. Clin. Invest. *125*, 727–738. https://doi.org/10.1172/JCI79651.

21. Georgiou, M., Fujinami, K., and Michaelides, M. (2020). Retinal imaging in inherited retinal diseases. Ann. Eye Sci. *5*, 25. https://doi.org/10.21037/aes-20-81.

22. Maguire, A.M., Russell, S., Chung, D.C., Yu, Z.F., Tillman, A., Drack, A.V., Simonelli, F., Leroy, B.P., Reape, K.Z., High, K.A., and Bennett, J. (2021). Durability of Voretigene Neparvovec for Biallelic RPE65-Mediated Inherited Retinal Disease: Phase 3 Results at 3 and 4 Years. Ophthalmology *128*, 1460–1468. https://doi.org/10.1016/j.ophtha.2021.03.031.

23. Redmond, T.M., Yu, S., Lee, E., Bok, D., Hamasaki, D., Chen, N., Goletz, P., Ma, J.X., Crouch, R.K., and Pfeifer, K. (1998). Rpe65 is necessary for production of 11-cis-vitamin A in the retinal visual cycle. Nat. Genet. *20*, 344–351. https://doi.org/10.1038/3813.

24. Choi, V.W., Bigelow, C.E., McGee, T.L., Gujar, A.N., Li, H., Hanks, S.M., Vrouvlianis, J., Maker, M., Leehy, B., Zhang, Y., et al. (2015). AAV-mediated RLBP1 gene therapy improves the rate of dark adaptation in Rlbp1 knockout mice. Mol. Ther. Methods Clin. Dev. *2*, 15022. https://doi.org/10.1038/mtm.2015.22.

25. Cereso, N., Pequignot, M.O., Robert, L., Becker, F., De Luca, V., Nabholz, N., Rigau, V., De Vos, J., Hamel, C.P., and Kalatzis, V. (2014). Proof of concept for AAV2/5-mediated gene therapy in iPSc-derived retinal pigment epithelium of choroideremia patients. Mol. Ther. Methods Clin. Dev. *1*, 14011. https://doi.org/10.1038/mtm.2014.11.

26. Torriano, S., Erkilic, N., Faugere, V., Damodar, K., Hamel, C.P., Roux, A.F., and Kalatzis, V. (2017). Pathogenicity of a novel missense variant associated with choroideremia and its impact on gene replacement therapy. Hum. Mol. Genet. *26*, 3573–3584. https://doi.org/10.1093/hmg/ddx244.

27. Sonoda, S., Spee, C., Barron, E., Ryan, S.J., Kannan, R., and Hinton, D.R. (2009). A protocol for the culture and differentiation of highly polarized human retinal pigment epithelial cells. Nat. Protoc. *4*, 662–673. https://doi.org/10.1038/nprot.2009.33.

28. Bocquet, B., Borday, C., Erkilic, N., Mamaeva, D., Donval, A., Masson, C., Parain, K., Kaminska, K., Quinodoz, M., Perea-Romero, I., et al. (2023). TBC1D32 variants disrupt retinal ciliogenesis and cause retinitis pigmentosa. JCI Insight *8*, e169426. https://doi.org/10.1172/jci.insight.169426.

29. Saari, J.C., Bredberg, D.L., and Noy, N. (1994). Control of substrate flow at a branch in the visual cycle. Biochemistry *33*, 3106–3112. https://doi.org/10.1021/bi00176a045.

30. Imanishi, Y., Gerke, V., and Palczewski, K. (2004). Retinosomes: new insights into intracellular managing of hydrophobic substances in lipid bodies. J. Cell Biol. *166*, 447–453. https://doi.org/10.1083/jcb.200405110.

31. Palczewska, G., Maeda, T., Imanishi, Y., Sun, W., Chen, Y., Williams, D.R., Piston, D.W., Maeda, A., and Palczewski, K. (2010). Noninvasive multiphoton fluorescence microscopy resolves retinol and retinal condensation products in mouse eyes. Nat. Med. *16*, 1444–1449. https://doi.org/10.1038/nm.2260.

32. Mamaeva, D., Jazouli, Z., DiFrancesco, M.L., Erkilic, N., Dubois, G., Hilaire, C., Meunier, I., Boukhaddaoui, H., and Kalatzis, V. (2021). Novel roles for voltage-gated T-type Ca^{2+} and ClC-2 channels in phagocytosis and angiogenic factor balance identified in human iPSC-derived RPE. FASEB J. *35*, e21406. https://doi.org/10.1096/fj.202002754R.

33. Guignard, T.J., Jin, M., Pequignot, M.O., Li, S., Chassigneux, Y., Chekroud, K., Guillou, L., Richard, E., Hamel, C.P., and Brabet, P. (2010). FATP1 inhibits 11-cis retinol formation via interaction with the visual cycle retinoid isomerase RPE65 and lecithin:retinol acyltransferase. J. Biol. Chem. *285*, 18759–18768. https://doi.org/10.1074/jbc.M109.064329.

34. Georgiou, M., Fujinami, K., and Michaelides, M. (2021). Inherited retinal diseases: Therapeutics, clinical trials and end points-A review. Clin. Exp. Ophthalmol. *49*, 270–288. https://doi.org/10.1111/ceo.13917.

35. Bunt-Milam, A.H., and Saari, J.C. (1983). Immunocytochemical localization of two retinoid-binding proteins in vertebrate retina. J. Cell Biol. *97*, 703–712. https://doi.org/10.1083/jcb.97.3.703.

36. Wenzel, A., Reme, C.E., Williams, T.P., Hafezi, F., and Grimm, C. (2001). The Rpe65 Leu450Met variation increases retinal resistance against light-induced degeneration by slowing rhodopsin regeneration. J. Neurosci. *21*, 53–58. https://doi.org/10.1523/JNEUROSCI.21-01-00053.2001.

37. Chen, S., Samuel, W., Fariss, R.N., Duncan, T., Kutty, R.K., and Wiggert, B. (2003). Differentiation of human retinal pigment epithelial cells into neuronal phenotype by N-(4-hydroxyphenyl)retinamide. J. Neurochem. *84*, 972–981. https://doi.org/10.1046/j.1471-4159.2003.01608.x.

38. Farjo, K.M., Moiseyev, G., Takahashi, Y., Crouch, R.K., and Ma, J.X. (2009). The 11-cis-retinol dehydrogenase activity of RDH10 and its interaction with visual cycle proteins. Invest. Ophthalmol. Vis. Sci. *50*, 5089–5097. https://doi.org/10.1167/iovs.09-3797.

39. Wen, B., Li, S., Li, H., Chen, Y., Ma, X., Wang, J., Lu, F., Qu, J., and Hou, L. (2016). Microphthalmia-associated transcription factor regulates the visual cycle genes Rlbp1 and Rdh5 in the retinal pigment epithelium. Sci. Rep. *6*, 21208. https://doi.org/10.1038/srep21208.

40. Ferrington, D.A., Ebeling, M.C., Kapphahn, R.J., Terluk, M.R., Fisher, C.R., Polanco, J.R., Roehrich, H., Leary, M.M., Geng, Z., Dutton, J.R., and Montezuma, S.R. (2017). Altered bioenergetics and enhanced resistance to oxidative stress in human retinal pigment epithelial cells from donors with age-related macular degeneration. Redox Biol. *13*, 255–265. https://doi.org/10.1016/j.redox.2017.05.015.

41. Wenzel, A., Oberhauser, V., Pugh, E.N., Jr., Lamb, T.D., Grimm, C., Samardzija, M., Fahl, E., Seeliger, M.W., Remé, C.E., and von Lintig, J. (2005). The retinal G protein-coupled receptor (RGR) enhances isomerohydrolase activity independent of light. J. Biol. Chem. *280*, 29874–29884. https://doi.org/10.1074/jbc.M503603200.

42. Collery, R., McLoughlin, S., Vendrell, V., Finnegan, J., Crabb, J.W., Saari, J.C., and Kennedy, B.N. (2008). Duplication and divergence of zebrafish CRALBP genes uncovers novel role for RPE- and Muller-CRALBP in cone vision. Invest. Ophthalmol. Vis. Sci. *49*, 3812–3820. https://doi.org/10.1167/iovs.08-1957.

43. Crabb, J.W., Carlson, A., Chen, Y., Goldflam, S., Intres, R., West, K.A., Hulmes, J.D., Kapron, J.T., Luck, L.A., Horwitz, J., and Bok, D. (1998). Structural and functional characterization of recombinant human cellular retinaldehyde-binding protein. Protein Sci. *7*, 746–757. https://doi.org/10.1002/pro.5560070324.

44. Saari, J.C., and Crabb, J.W. (2005). Focus on molecules: cellular retinaldehyde-binding protein (CRALBP). Exp. Eye Res. *81*, 245–246. https://doi.org/10.1016/j.exer.2005.06.015.

45. Bonilha, V.L., Bhattacharya, S.K., West, K.A., Crabb, J.S., Sun, J., Rayborn, M.E., Nawrot, M., Saari, J.C., and Crabb, J.W. (2004). Support for a proposed retinoid-processing protein complex in apical retinal pigment epithelium. Exp. Eye Res. *79*, 419–422. https://doi.org/10.1016/j.exer.2004.04.001.

46. Nawrot, M., West, K., Huang, J., Possin, D.E., Bretscher, A., Crabb, J.W., and Saari, J.C. (2004). Cellular retinaldehyde-binding protein interacts with ERM-binding phosphoprotein 50 in retinal pigment epithelium. Invest. Ophthalmol. Vis. Sci. *45*, 393–401. https://doi.org/10.1167/iovs.03-0989.

47. Bassetto, M., Kolesnikov, A.V., Lewandowski, D., Kiser, J.Z., Halabi, M., Einstein, D.E., Choi, E.H., Palczewski, K., Kefalov, V.J., and Kiser, P.D. (2024). Dominant role for pigment epithelial CRALBP in supplying visual chromophore to photoreceptors. Cell Rep. *43*, 114143. https://doi.org/10.1016/j.celrep.2024.114143.

48. Schlegel, D.K., Ramkumar, S., von Lintig, J., and Neuhauss, S.C. (2021). Disturbed retinoid metabolism upon loss of *rlbp1a* impairs cone function and leads to subretinal lipid deposits and photoreceptor degeneration in the zebrafish retina. Elife *10*, e71473. https://doi.org/10.7554/eLife.71473.

49. Maguire, A.M., Simonelli, F., Pierce, E.A., Pugh, E.N., Jr., Mingozzi, F., Bennicelli, J., Banfi, S., Marshall, K.A., Testa, F., Surace, E.M., et al. (2008). Safety and efficacy of gene transfer for Leber's congenital amaurosis. N. Engl. J. Med. *358*, 2240–2248. https://doi.org/10.1056/NEJMoa0802315.

50. Bainbridge, J.W.B., Smith, A.J., Barker, S.S., Robbie, S., Henderson, R., Balaggan, K., Viswanathan, A., Holder, G.E., Stockman, A., Tyler, N., et al. (2008). Effect of gene therapy on visual function in Leber's congenital amaurosis. N. Engl. J. Med. *358*, 2231–2239. https://doi.org/10.1056/NEJMoa0802268.

51. Bennett, J. (2017). Taking Stock of Retinal Gene Therapy: Looking Back and Moving Forward. Mol. Ther. *25*, 1076–1094. https://doi.org/10.1016/j.ymthe.2017.03.008.

52. Kennedy, B.N., Li, C., Ortego, J., Coca-Prados, M., Sarthy, V.P., and Crabb, J.W. (2003). CRALBP transcriptional regulation in ciliary epithelial, retinal Muller and retinal pigment epithelial cells. Exp. Eye Res. *76*, 257–260. https://doi.org/10.1016/s0014-4835(02)00308-1.

53. Lima de Carvalho, J.R., Jr., Kim, H.J., Ueda, K., Zhao, J., Owji, A.P., Yang, T., Tsang, S.H., and Sparrow, J.R. (2020). Effects of deficiency in the *RLBP1*-encoded visual cycle protein CRALBP on visual dysfunction in humans and mice. J. Biol. Chem. *295*, 6767–6780. https://doi.org/10.1074/jbc.RA120.012695.

54. Huang, J., Possin, D.E., and Saari, J.C. (2009). Localizations of visual cycle components in retinal pigment epithelium. Mol. Vis. *15*, 223–234.

55. Golovleva, I., Bhattacharya, S., Wu, Z., Shaw, N., Yang, Y., Andrabi, K., West, K.A., Burstedt, M.S.I., Forsman, K., Holmgren, G., et al. (2003). Disease-causing mutations in the cellular retinaldehyde binding protein tighten and abolish ligand interactions. J. Biol. Chem. *278*, 12397–12402. https://doi.org/10.1074/jbc.M207300200.

56. He, X., Lobsiger, J., and Stocker, A. (2009). Bothnia dystrophy is caused by domino-like rearrangements in cellular retinaldehyde-binding protein mutant R234W. Proc. Natl. Acad. Sci. USA *106*, 18545–18550. https://doi.org/10.1073/pnas.0907454106.

57. Sanjurjo-Soriano, C., Erkilic, N., Damodar, K., Boukhaddaoui, H., Diakatou, M., Garita-Hernandez, M., Mamaeva, D., Dubois, G., Jazouli, Z., Jimenez-Medina, C., et al. (2022). Retinoic acid delays initial photoreceptor differentiation and results in a highly structured mature retinal organoid. Stem Cell Res. Ther. *13*, 478. https://doi.org/10.1186/s13287-022-03146-x.

58. Simonin, Y., Erkilic, N., Damodar, K., Clé, M., Desmetz, C., Bolloré, K., Taleb, M., Torriano, S., Barthelemy, J., Dubois, G., et al. (2019). Zika virus induces strong inflammatory responses and impairs homeostasis and function of the human retinal pigment epithelium. EBioMedicine *39*, 315–331. https://doi.org/10.1016/j.ebiom.2018.12.010.

59. Hirtz, C., Mannaa, A.M., Moulis, E., Pible, O., O'Flynn, R., Armengaud, J., Jouffret, V., Lemaistre, C., Dominici, G., Martinez, A.Y., et al. (2022). Deciphering Black Extrinsic Tooth Stain Composition in Children Using Metaproteomics. ACS Omega *7*, 8258–8267. https://doi.org/10.1021/acsomega.1c04770.

60. Rydzanicz, R., Zhao, X.S., and Johnson, P.E. (2005). Assembly PCR oligo maker: a tool for designing oligodeoxynucleotides for constructing long DNA molecules for RNA production. Nucleic Acids Res. *33*, W521–W525. https://doi.org/10.1093/nar/gki380.

61. Muniz, A., Greene, W.A., Plamper, M.L., Choi, J.H., Johnson, A.J., Tsin, A.T., and Wang, H.C. (2014). Retinoid uptake, processing, and secretion in human iPS-RPE support the visual cycle. Invest Ophthalmol. Vis. Sci. *55*, 198–209. https://doi.org/10.1167/iovs.13-11740.

62. Suzuki, T., Fujita, Y., Noda, Y., and Miyata, S. (1986). A simple procedure for the extraction of the native chromophore of visual pigments: the formaldehyde method. Vis. Res. *26*, 425–429. https://doi.org/10.1016/0042-6989(86)90185-9.

63. Chekroud, K., Arndt, C., Basset, D., Hamel, C.P., Brabet, P., and Pequignot, M.O. (2011). Simple and efficient: validation of a cotton wick electrode for animal electroretinography. Ophthalmic Res. *45*, 174–179. https://doi.org/10.1159/000321118.

YMTHE, Volume *32*

Supplemental Information

Dual CRALBP isoforms unveiled: iPSC-derived retinal modeling and AAV2/5-RLBP1 gene transfer raise considerations for effective therapy

Krishna Damodar, Gregor Dubois, Laurent Guillou, Daria Mamaeva, Marie Pequignot, Nejla Erkilic, Carla Sanjurjo-Soriano, Hassan Boukhaddaoui, Florence Bernex, Béatrice Bocquet, Jérôme Vialaret, Yvan Arsenijevic, T. Michael Redmond, Christopher Hirtz, Isabelle Meunier, Philippe Brabet, and Vasiliki Kalatzis

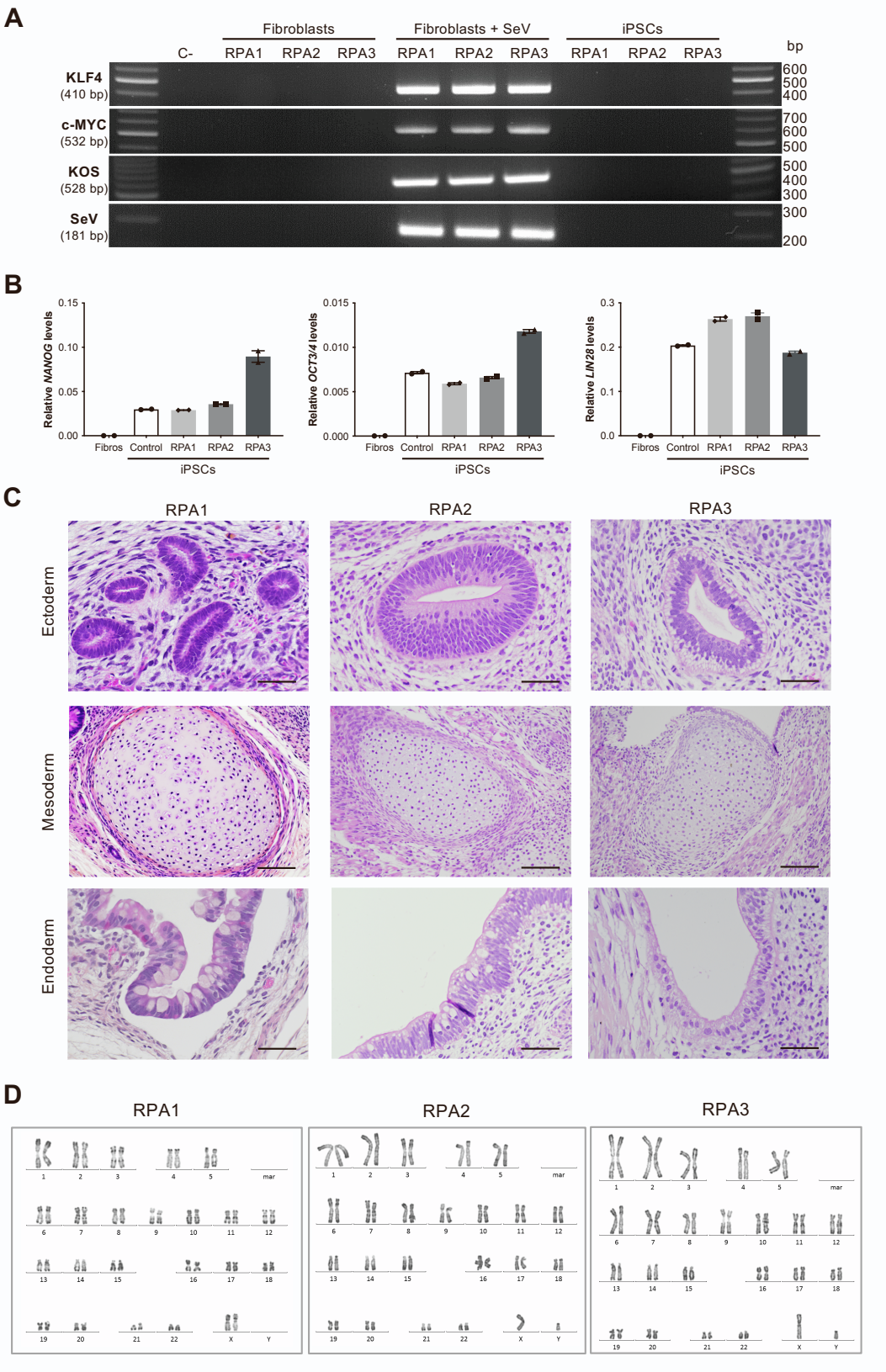
A
Fibroblasts
Fibroblasts + SeV
iPSCs
C-
RPA1
RPA2
RPA3
RPA1
RPA2
RPA3
RPA1
RPA2
RPA3
bp
KLF4
(410 bp)
600
500
400
c-MYC
(532 bp)
700
600
500
KOS
(528 bp)
500
400
300
SeV
(181 bp)
300
200
B
Relative NANOG levels
0.15
0.10
0.05
0.00
Fibros
Control
RPA1
RPA2
RPA3
iPSCs
Relative OCT3/4 levels
0.015
0.010
0.005
0.000
Fibros
Control
RPA1
RPA2
RPA3
iPSCs
Relative LIN28 levels
0.3
0.2
0.1
0.0
Fibros
Control
RPA1
RPA2
RPA3
iPSCs
C
RPA1
RPA2
RPA3
Ectoderm
Mesoderm
Endoderm
D
RPA1
RPA2
RPA3

Figure S1: Quality controls of RPA1, RPA2 and RPA3 iPSCs. A) RT-PCR analysis of the clearance of the Sendai virus (SeV) reprogramming vectors in iPSCs at P12 (RPA2) and P16 (RPA1 and RPA3) using primers specific to the transgene cassettes (KLF4, c-MYC, KOS) or viral backbone (SeV). C-, control without cDNA; Fibroblasts, negative control; SeV-transduced fibroblasts (+ SeV), positive control. **B**) qPCR analysis of the relative expression of host pluripotency genes *NANOG*, *OCT3/4* and *LIN28A* in control iPSCs (positive control) and iPSCs of RPA1, RPA2 and RPA3 patients; Fibroblasts (Fibros), negative control. **C**) Teratoma assay showing the differentiation of RPA1, RPA2 and RPA3 iPSCs into: ectoderm, as determined by the presence of neural tubes (row 1); mesoderm, as determined by the presence of cartilage (row 2); endoderm, as determined by the presence of intestinal epithelium with typical mucous cells (row 3). Scale bar = 50 µm (ectoderm and endoderm) and 100 µm (mesoderm). **D**) Karyotype analysis of RPA1 iPSCs with a normal 46, XX karyotype at P16, and RPA2 and RPA3 iPSCs with a normal 46, XY karyotype at P14 and P19, respectively.

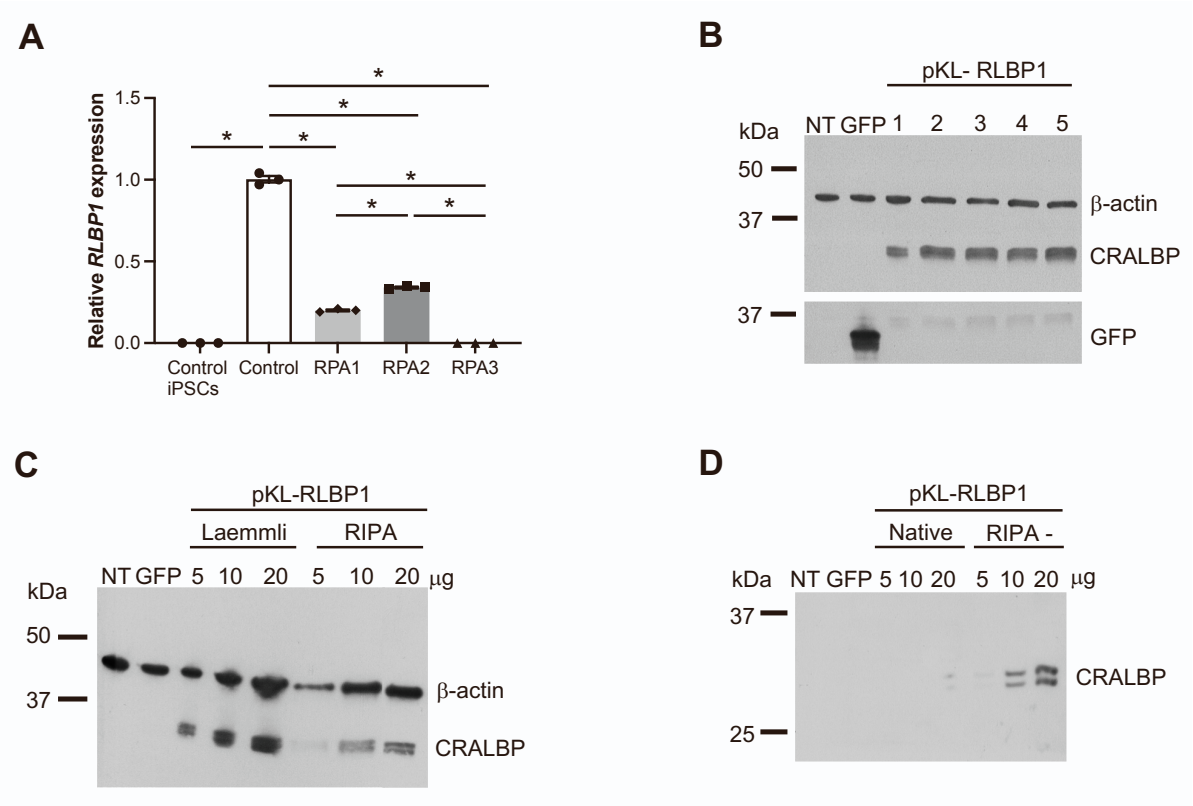

Figure S2: *RLBP1* in iPSC-derived RPE and CRALBP expression from proviral plasmids. A) qPCR analysis of *RLBP1* expression in control iPSCs, and in control, RPA1, RPA2 and RPA3 iPSC-derived RPE using a forward primer spanning the exon 6 to 7 junction and a reverse primer in exon 7 (situated in the deletion carried by RPA3). Data are represented as mean ± SEM and expressed relative to control; *p<0.05; n = 3. **B**) Western blot analysis of CRALBP using a mouse monoclonal antibody in COS-7 cells non-transfected (NT), or transfected with a GFP-expressing plasmid or pKL-RLBP1, and scraped and collected in different combinations of protein inhibitor cocktails (PIC) and buffers: 1. Roche PIC and resuspension in Laemmli buffer (standard conditions); 2. Roche PIC and lysis in RIPA buffer; 3. Cell signalling PIC and lysis in Cell signalling lysis buffer; 4. Cell signalling PIC and lysis in RIPA buffer; 5. Roche PIC and lysis in Cell Signalling buffer; β-actin was used as loading control and GFP as a positive transfection control. **C**) Western blot analysis of CRALBP using a mouse monoclonal antibody in COS-7 cells NT or transfected with a GFP-expressing plasmid or pKL-RLBP1, and collected in Laemmli or RIPA buffer; β-actin was the loading control. **D**) Western blot analysis of CRALBP using a mouse polyclonal antibody in COS-7 cells NT or transfected with a GFP-expressing plasmid or with pKL-RLBP1, collected in Biorad Native sample buffer or lysed in RIPA (without SDS) buffer, and migrated under non-denaturing conditions; β-actin was the loading control.

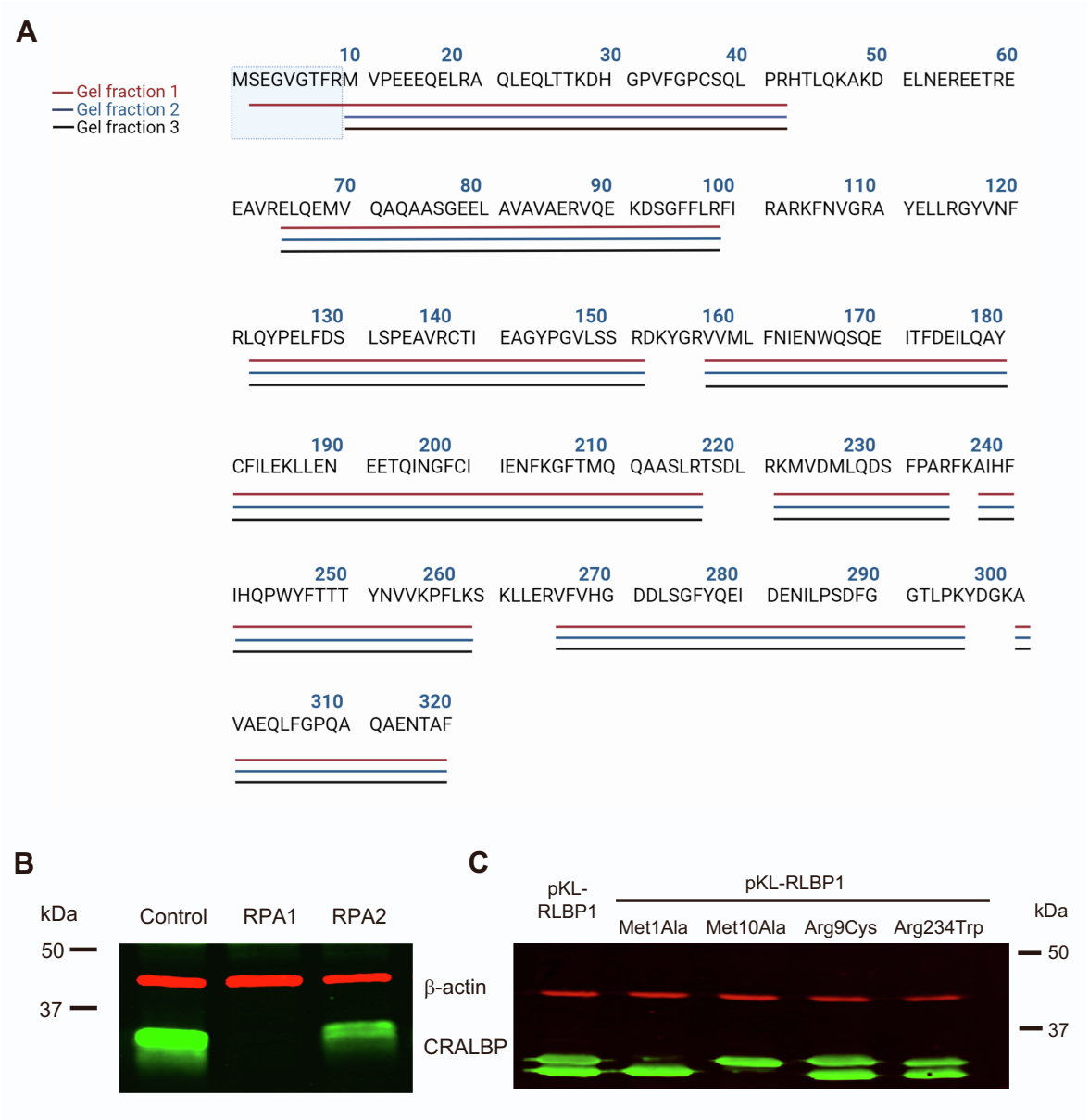

Figure S3: Proteomic and western blot analysis of control or mutant CRALBP isoforms. Alignment of the CRALBP peptides identified by mass spectrometry in the different gel fractions on the full length CRALBP sequence. The light blue square indicates the differing N-terminus between the two isoforms. **B**) Western blot analysis of CRALBP in 30 µg lysate of control, RPA1 and RPA2 iPSC-derived RPE cultured in 24-well plates. **C**) Western blot analysis of the CRALBP isoforms in 15 µg lysates of HEK-293 cells transfected with the control pKL-RLBP1 plasmid and the plasmids mutated in the ATG start codons (Met1Ala, Met10Ala) or carrying the missense variants present in patients RPA1 (Arg234Trp) and RPA2 (Arg9Cys); β-actin was the loading control in B and C.

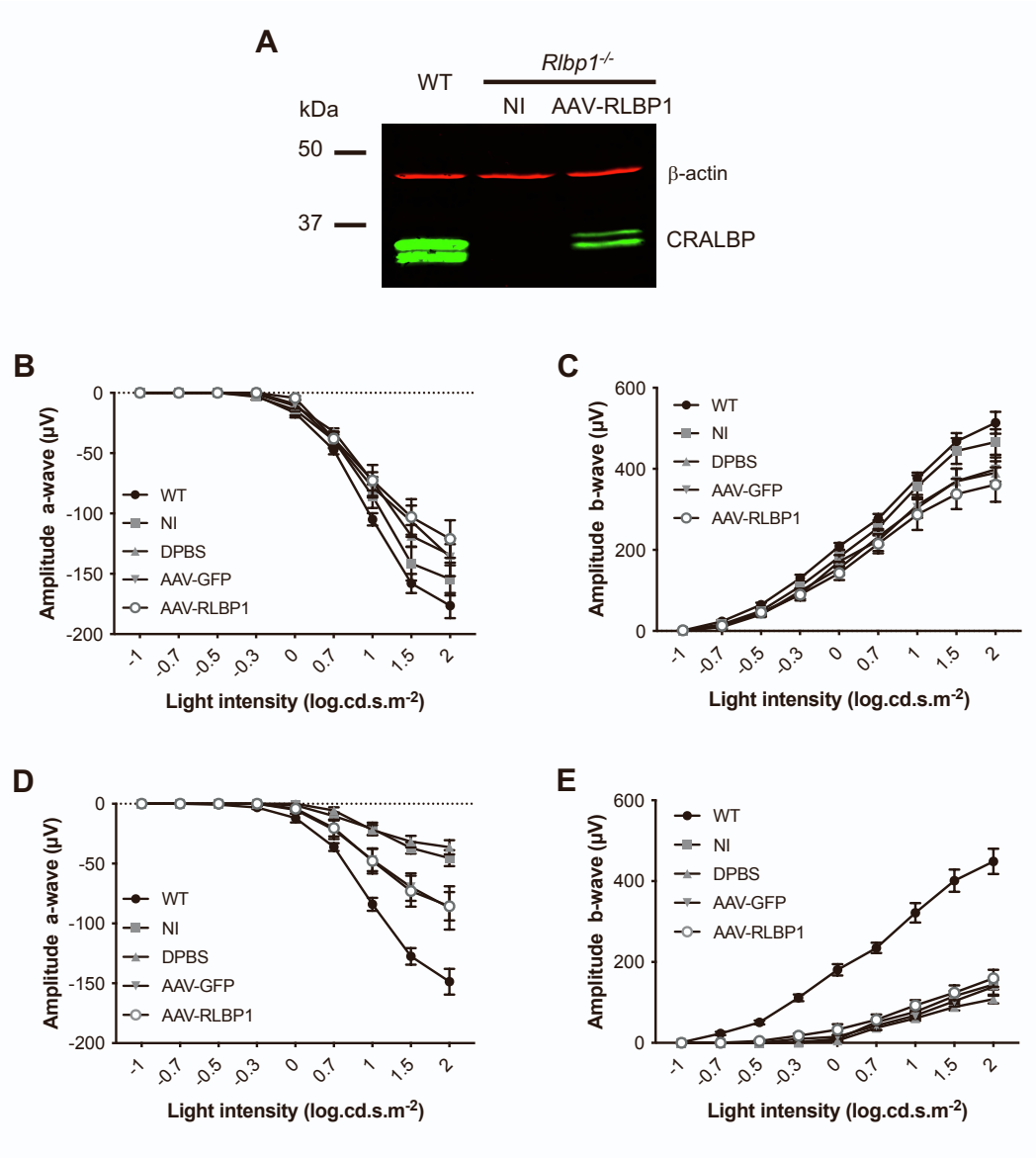

Figure S4: CRALBP production and scotopic ERG recordings post-AAV-RLBP1 administration. Western blot analysis of CRALBP in the eyes of wild-type (WT) and non-injected (NI) or AAV-RLBP1-injected *Rlbp1*$^{-/-}$ mice; β-actin represents the loading control. Baseline a-wave (**B**) and b-wave (**C**) ERG amplitudes (in μV) in dark-adapted WT and NI, DPBS-injected, AAV-GFP-injected and AAV-RLBP1-injected *Rlbp1*$^{-/-}$ mice following stimulation at increasing light intensities expressed in log candela second/metre^2. Recordings were performed up to 8 weeks post-injection. Data are represented as mean ± SEM; *n* = 9 (WT), 10 (NI), 9 (DPBS), 7 (AAV-GFP) and 8 (AAV-RLBP1). a-wave (**D**) and b-wave (**E**) ERG amplitudes post-photobleaching of the same wild type (WT) and *Rlbp1*$^{-/-}$ mice recorded up to 10 weeks post-treatment. Data are represented as mean ± SEM.

Table S1. PCR, sequencing, genotyping and mutagenesis primers

Target	Experiment	Sequence (5' to 3')
*Mlu*I-*RLBP1*	Vector production	F: **ACG CGT** ATG TCA GAA GGG GTG GGC AC
*RLBP1-Xho*I		R: **CTC GAG** TCA GAA GGC TGT GTT CTC AG
pKL backbone	Sanger sequencing cDNA	F: AAT CTG TGC GGA GCC GAA AT
RLBP1 exon 5		F: CGC GCA CGG AAG TTC AAC GT
RLBP1 exon 7		F: CAA GGG CTT TAC CAT GCA GC
RLBP1 exon 5		R: GAA GCC GCT GTC CTT CTC TT
RLBP1 exon 6		R: AGG CTG TCA AAG AGC TCA GG
RLBP1 exon 7-8		R: TCC TGG AGC ATG TCC ACC AT
Rlbp1	Genotyping	F: TTA GAC TCA CAG GGG CCA ACA
		R1: ATG ATC CTT GGT TGT GAG CTG CTC
		R2: TAA AGC GCA TGC TCC AGA CT
c.1ATG>GCG	Site directed mutagenesis	F: TTC GAG CGA ACG CGT **GCG** TCA GAA GGG GTG GG
p.Met1Ala		R: CCC ACC CCT TCT GAC GCA CGC GTT CGC TCG AA
c.28ATG>GCG	Overlapping PCR	F1: TGA TTA ATT CGA GCG AAC GCG T**AT G**TC AGA AGG GGT GGG CAC GTT CCG
p.Met10Ala		R2: CAG TTG GGC ACG GAG CTC CTG TTC CTC TTC AGG TAC **CGC** GCG GAA CGT GCC CAC C
		F3: GCT CCG TGC CCA ACT GGA GCA GCT CAC AAC CAA GGA CCA TGG ACC TGT CTT TGG CCC
		R4: CTT GGC CTT CTG CAA GGT GTG GCG GGG CAG CTG GCT GCA CGG GCC AAA GAC AGG TCC
		F5: ACC TTG CAG AAG GCC AAG GAT GAG CTG AAC GAG AGA GAG GAG ACC CGG GAG GAG GC
		R6: TGC GCC TGC ACC ATC TCC TGC AGC TCT CGC ACT GCC TCC TCC CGG G
	Flanking PCR	F: TGA TTA ATT CGA GCG AAC GCG
		R: TGC GCC TGC ACC ATC
c.25C>T	Site directed mutagenesis	F: GGG TGG GCA CGT TCT GCA TGG TAC CTG AAR'
p.Arg9Cys		R: 5'TTC AGG TAC CAT GCA GAA CGT GCC CAC CC3
c.700C>T	Site directed mutagenesis	F: GAT TCC TTC CCA GCC TGG TTC AAA GCC ATCC
p.Arg234Trp		R: GGA TGG CTT TGA ACC AGG CTG GGA AGG AAT C
c.25C>T in exon 4	Sanger sequencing gDNA	F: GAC CCC ACA AAA GGA GGA GG
(p.Arg9Cys; RPA2)		R: GCT GGA CCC TTT TCA CAG GA
c.333T>G in exon 5	Sanger sequencing gDNA	F: CCT CAC CCG CAC CTA AGT TT
(p.Tyr111X; RPA1 and RPA2)		R: GGG GGT CTG GAG GGG AAA TT
c.700C>T in exon 8	Sanger sequencing gDNA	F: TTG CTG GCC TGG AAA TAG GA
(p.Arg234Trp; RPA1)		R: GGT GCC CTA AGG ATG AGG GT
Exons 7-9del (RPA3)	Long-range PCR (gDNA)	F: TGT GAA GCT GAG CAC GTC AGA T
		R: TTG GGA GAA CTT TGG CAT G

F – forward, R – reverse

Table S2. RT-PCR and qPCR primer sequences

Target	Experiment	Forward primer	Reverse primer	Efficacity
RLBP1	qPCR exons 6-7	GAA ATC ACC TTT GAT GAG AT	TCT TCC TGA GAT CTG AAG TC	2.18
RLBP1	qPCR exon 6	ACC CTG AGC TCT TTG ACA GC	TGA AGA GCA TGA CCA CTC GG	2.02
SeV	RT-PCR	GGA TCA CTA GGT GAT ATC GAG C	ACC AGA CAA GAG TTT AAG AGA TAT GTA TC	N/A
KOS	RT-PCR	ATG CAC CGC TAC GAC GTG AGC GC	ACCTTGACAATCCTGATGTGG	N/A
KLF4	RT-PCR	TTC CTG CAT GCC AGA GGA GCC C	AAT GTA TCG AAG GTGCTC AA	N/A
c-MYC	RT-PCR	TAA CTG ACT AGC AGG CTT GTC G	TCC ACA TAC AGT CCT GGA TGA TGA TG	N/A
NANOG	qPCR	CAA AGG CAA ACA ACC CAC TT	TCT GCT GGA GGC TGA GGT AT	2.06
OCT3/4	qPCR	GTA CTC CTC GGT CCC TTT CC	CAA AAA CCC TGG CAC AAA CT	1.94
LIN28A	qPCR	GGG GAA TCA CCC TAC AAC CT	CTT GGC TCC ATG AAT CTG GT	2.16
GAPDH	qPCR	AAC CAT GAG AAG TAT GAC AAC	CTT CCA CGA TAC CAA AGT T	2.02
L27	qPCR	ACG CAA AGC CGT CAT CGT GAA G	CTT GGC GAT CTT CTT CTT GCC	2.09

N/A – non-applicable

Table S3: Primary antibodies

Primary antibodies	Host	Clonality	Dilution	Company	Cat #
anti-ARL13B	Rabbit	Polyclonal	1/3000	Proteintech	17711-1-AP
anti-β-actin, clone AC-74	Mouse	Monoclonal	1/10000	Sigma-Aldrich	A5316
anti-BEST1	Mouse	Monoclonal	1/500	Abcam	Ab2182
anti-CRALBP, clone B2	Mouse	Monoclonal	1/1000	Abcam	ab15051
anti-CRALBP	Rabbit	Monoclonal	1/1000	Abcam	ab183728
anti-CRALBP	Mouse	Polyclonal	1/1000	AgroBio	Directed against recombinant human CRALBP
anti-GFP	Rabbit	Polyclonal	1/2000	Invitrogen	A6455
anti-LRAT	Rabbit	Polyclonal	1/250	Abcam	ab166784
anti-MERTK, clone Y323	Rabbit	Monoclonal	1/250	Abcam	ab52968
anti-Perilipin-2	Guinea pig	Polyclonal	1/2000	Progen	GP47
anti-RPE65	Mouse	Monoclonal	1/1000	Abcam	ab13826
anti-ZO-1	Rabbit	Polyclonal	1/100	ThermoFisher Scientific	40-2200

Table S4: Secondary antibodies

Secondary antibodies	Host	Dilution	Company	Cat #
anti-Mouse IgG-HRP	Sheep	1/10000 (WB)	Jackson ImmunoResearch	515-035-003
anti-Guinea Pig-HRP	Goat	1/10000 (WB)	Jackson ImmunoResearch	106-035-003
anti-Mouse IgG IRDye 680RD	Donkey	1/20000 (WB)	LI-COR Biosciences	926-68072
anti-Rabbit IgG IRDye 800CW	Donkey	1/20000 (WB)	LI-COR Biosciences	926-32213
anti-Mouse IgG Alexa Fluor 488	Donkey	1/500	ThermoFisher Scientific	A-21202
anti-Mouse IgG Alexa Fluor 594	Donkey	1/500	ThermoFisher Scientific	A-21203
anti-Rabbit IgG Alexa Fluor 488	Donkey	1/500	ThermoFisher Scientific	A-21206
anti-Rabbit IgG Alexa Fluor 594	Donkey	1/500	ThermoFisher Scientific	A-21207
anti-Mouse IgG Alexa Fluor 546	Goat	1/500	ThermoFisher Scientific	A10036
anti-Mouse IgG Alexa Fluor 594 AffiniPure	Donkey	1/500	Jackson ImmunoResearch	715-585-150
anti-Rabbit IgG Alexa Fluor 594 AffiniPure	Donkey	1/500	Jackson ImmunoResearch	711-585-152
anti-Mouse IgG Alexa Fluor 488 AffiniPure	Donkey	1/500	Jackson ImmunoResearch	715-546-151
anti-Rabbit IgG Alexa Fluor 488 AffiniPure	Donkey	1/500	Jackson ImmunoResearch	711-545-152